JOHNSON-MEHL-AVRAMI KINETICS OF INTRACELLULAR ICE FORMATION IN CONFLUENT TISSUE CONSTRUCTS

A Thesis
Presented to
The Academic Faculty

by

Megan L. Sumpter

In Partial Fulfillment
of the Requirements for the Degree
Master of Science in the
School of Mechanical Engineering

Georgia Institute of Technology
July 2004

JOHNSON-MEHL-AVRAMI KINETICS OF INTRACELLULAR ICE FORMATION IN CONFLUENT TISSUE CONSTRUCTS

Approved by:

Dr. Jens O. M. Karlsson, advisor
Dr. Andrei G. Fedorov
Dr. Mo Li
Dr. Thomas H. Sanders, Jr.

Date Approved: April, 23, 2004

ACKNOWLEDGMENTS

I would like to thank my thesis advisor, Dr. Jens O.M. Karlsson, for his guidance and impressive skill in scientific research. I would also like to thank my thesis committee members Dr. Andrei G. Fedorov, Dr. Mo Li, and Dr. Thomas H. Sanders, Jr. for their insight and recommendations for my work.

I would like to thank my colleague Shannon Stott for her patient instruction in laboratory techniques, and my fellow labmates in the Biothermal Sciences Laboratory, Adam Higgins and Kevin Carnevale, for their support and encouragement.

I would also like to especially thank Anthony Dickherber for his support, love, and unwavering confidence in my abilities.

This work was funded in part by National Science Foundation Grant # BES-0242377.

TABLE OF CONTENTS

TABLE OF CONTENTS (CONTINUED)

LIST OF FIGURES

LIST OF FIGURES (CONTINUED)

LIST OF FIGURES (CONTINUED)

LIST OF SYMBOLS

α	Non-dimensional intercellular ice propagation rate
β	Daughter phase described by transformation kinetics
τ	Non-dimensional time with respect to J_i
τ_p	Non-dimensional time with respect to J_p
χ^2	Chi-squared statistic
a_0	Overall rate of IIF in a tissue in Gillespie's algorithm
c	Coefficient for phenomenological 2-D JMA model
c_j	Rate of conversion in cell *j* from unfrozen to frozen
h_j	State parameter in Gillespie's algorithm
IIF	Intracellular ice formation
J	Average rate of intracellular ice formation
J_i	Spontaneous independent ice nucleation rate
J^j_{IIF}	Rate of IIF in cell *j*
JMA	Johnson-Mehl-Avrami model
J_n	Average rate of nucleation per unite volume
J_p	Ice propagation rate in tissues
k	Avrami coefficient
k_j	Number of frozen nearest neighbors of cell *j*
$\bar{k}$	Average number of interfaces for propagation
m	Exponent for phenomenological 2-D JMA model
n	Avrami exponent
n_{cells}	Total number of cells in a tissue
n_0	Number of frozen cells in a cluster
n_{IIF}	Number of cells with intracellular ice formation
$n_{IIF}{}^e$	Number of frozen cells in a tissue neglecting impingment
N_n	Number of frozen nuclei in a tissue
P	Seeding probability for Weinberg-Kapral discrete nucleation case
p^j_{IIF}	Probability that cell *j* is frozen

LIST OF SYMBOLS (CONTINUED)

P_{IIF}	Probability of IIF or transformed fraction
P_{IIF}^{e}	Extended probability of IIF or extended transformed fraction
p	Gillespie's reaction probability density function
r	Seeding probability for Weinberg-Kapral continuous nucleation case
$\bar{t}$	Weinberg-Kapral time scale
t_n	Time a nucleation event occurs
V_{t_n}	Volume of a transformed region arising from a nucleation event at time t_n
V_β	Actual transformed volume
V_β^{e}	Extended transformed volume
V	Growth rate of a frozen nucleus
WK	Weinberg-Kapral model
X_β	Actual transformed fraction
X_β^{e}	Extended transformed fraction
Z	Probability of a site being untransformed in Weinberg-Kapral model

SUMMARY

In an effort to minimize the harmful effects of intracellular ice formation (IIF) during cryopreservation of confluent tissues, computer simulations based on Monte Carlo methods were performed to predict the probability of IIF in confluent monolayers during various freezing procedures. To overcome the prohibitive computational costs of such simulations for large tissues, the well-known Johnson-Mehl-Avrami (JMA) model of crystallization kinetics was implemented as a continuum approximation of IIF in tissues. This model, which describes nucleation, growth, and impingement of crystals in a supercooled melt, is analogous to the process of intracellular ice formation and propagation in biological tissues. Based on the work of Weinberg and Kapral (1989), the JMA model was modified to account for finite-size effects, and was shown to predict accurately the results of freezing simulations in 1-D tissue constructs, for various propagation rates and tissue sizes. An initial analysis of IIF kinetics in 2-D tissues is also presented. The probability of IIF in 2-D liver tissue was measured experimentally during freezing of HepG2 cells cultured in monolayers, and compared to Monte Carlo simulations and predictions of the continuum model. The Avrami coefficient and exponent for IIF in HepG2 tissue were estimated to be $k = 0.19$ and $n = 0.45$.

CHAPTER 1

INTRODUCTION

1.1 Need for Preservation in Tissue Engineering

Cryopreservation, the freezing of biological cells or tissues to cryogenic temperatures for purposes of long term storage in a state of "suspended animation" (allowing subsequent reanimation to a viable state), is a critical enabling technology for the production of tissue engineered, cell-based, medical devices (Karlsson and Toner, 2000). For example, source cells must be extensively tested for adventitious agents, a lengthy process during which the source cells must be preserved to prevent contamination or genotypic changes. Secondly, the US Food and Drug Administration requires the establishment of Master and Working Cell Banks which must be preserved under conditions that ensure genetic stability (Wiebe and May, 1990). Inventories of cells must be preserved long-term to give manufacturers the capacity for large-volume cell expansion with quick turn-around times in periods of high product demand. To assure quality control, samples of cells and tissues at each step of the production process need to be preserved and archived for documentation of each lot produced. As another example, shipping of engineered products requires stability in transit, and long-term preservation ensures the availability of the product to geographically distant markets. Lastly, preservation of tissues guarantees the availability of engineered devices to meet the unpredictable demand for tissues and organs in clinical settings.

Cryopreservation of cells and tissues offers many benefits over other methods of storage such as refrigeration, chemical preservation, and *in vitro* culture. These benefits

include long shelf-life with assured genetic stability, minimal risk of microbial contamination during storage, and improved cost effectiveness (for example, liquid nitrogen for cryogenic storage costs approximately $1/gallon, whereas serum for tissue culture costs more than $1000/gallon; Karlsson and Toner, 2000). Consequently, cryopreservation is the most advantageous strategy for meeting the requirements for production, distribution, and use of tissue-engineered products.

1.2 Cell Injury During Freezing

During the freezing process, cells are subject to physical damage by several mechanisms, including the deleterious sequelae of dehydration and ice crystalization. As the temperature decreases, ice will initially form in the extracellular solution. Cell dehydration is a response to osmotic forces resulting from the freeze-concentration of extracellular solutes due to depletion of liquid water via ice formation. During the dehydration process, the efflux of water makes the interior of the cell more concentrated in electrolytes (Mazur, 1963). Damage to cells can be caused by prolonged exposure to high intra- and extracellular solute concentrations; the corresponding mechanisms of cell injury are collectively referred to as "solution effects" in the cryobiology literature (Mazur, 1972).

The freezing process may also cause damage to cells as a result of intracellular ice formation (IIF). There are two opposing theories about the mechanism of injury associated with IIF: the more prevalent hypothesis is that the plasma membrane of the

cell is damaged by the formation of ice crystals inside the cell (Mazur, 1965); an alternative hypothesis posits that the plasma membrane is compromised due to damage sustained during the dehydration process allowing extracellular ice crystals to inoculate the cell cytoplasm (Muldrew and McGann, 1994). Per the former theory, ice crystals may form inside the cells via a process of nucleation (Toner, *et al*., 1990) *i.e.*, the spontaneous and random aggregation of water molecules into a solid phase as a result of the thermal fluctuations (Kashchiev, 2000). In any case, experimental evidence shows that intracellular ice crystal formation is highly correlated with irreversible cell damage (Toner, 1993).

The extent of cell injury during cryopreservation is highly dependent on the rate of cooling (Mazur, 1984). Dehydration is the dominant mechanism of damage to cells frozen at low cooling rates. Conversely, IIF is the dominant mode of injury at high cooling rates. Consequently, survival will be highest as some optimal intermediate cooling rate, which minimizes the effects of both modes of damage. A better understanding of the kinetics of IIF during freezing of cells or tissues will be necessary in order to develop successful cryopreservation procedures.

The response of tissues and organs during cryopreservation is significantly more complex than that of cell suspensions. For example, cell-cell interactions, cell-substrate adhesion, and phenotypic changes of cells during tissue culture can all affect the response to the freezing process (Karlsson and Toner, 2000; Irimia and Karlsson, 2002). In addition, due to the large scale of tissues and organs, cells may exhibit location-dependent responses to freezing as a result of heat- or mass-transfer limitations. For example, interior cells of tissues may be less prone to water loss as a result of the

additional transport barriers imposed by exterior cell layers (Karlsson and Toner, 2000, Levin, *et al*. 1977, Diller and Raymond, 1990). Consequently, design of cryopreservation protocols to optimize the post-thaw function of tissue constructs is even more challenging than the optimization of freezing procedures for cell suspensions.

1.3 Need for Modeling

Ever since Peter Mazur's seminal work in the early 1960s (Mazur, 1963), mathematical modeling has been recognized as an invaluable tool in the design of cryopreservation procedures. Whereas a practical cryopreservation protocol is characterized by multiple parameters (starting and ending temperatures, rates of cooling, concentration of additives, etc.), minimizing the harmful effects of dehydration and IIF can be difficult. Empirical optimization of these procedural details by factorial design is time-intensive and prohibitively expensive, whereas the number of required experiments grows exponentially with the number of protocol parameters. In addition, the optimization process must be repeated for each new cell type, due to species- and tissue-dependent variations in biophysical properties (Karlsson, *et al*., 1993). As a result of such differences, the optimum cooling rate can vary over several orders of magnitude between different cell species. For example, the critical cooling rate for mouse oocytes is less than 1ºC/min (Karlsson, *et al*., 1996), while the cooling rate for human red blood cells is in excess of 1000 ºC/min (Mazur 1984). Moreover, because the mechanisms of cell damage during cryopreservation are highly complex, the appropriate strategy for modifying a suboptimal freezing procedure in order to improve survival is usually not

clear from trends in experimental data alone. Mathematical models of the processes of dehydration and IIF can be helpful in interpretation of the experimentally observed trends in viability, but also make possible high throughput evaluation of candidate freezing protocols using computer simulations to predict outcome, and thus allow the design of cryopreservation procedures using optimization algorithms (Karlsson, *et al*., 1996).

1.4 Modeling of Cell Freezing

The earliest models of the cell's response to freezing focused on the water transport process that causes cell dehydration. The two-compartment, membrane-limited water transport model originally developed by Mazur (1963), and subsequently modified by Levin (1977a) is still widely used (*e.g.*, Schwartz and Diller, 1983; Rabin, *et al*., 1998; Zhao, *et al*., 2003; Boone, *et al*., 2004, Devireddy, *et al*., 2004). Typically, this model is coupled with a theoretical description of IIF, whereas the kinetics of IIF are strongly dependent on the cytoplasmic water content.

The development of theoretical models to predict IIF has been revived by Karlsson *et al*. (1993). The first theoretical treatment was a simple phenomenological model with predicted the probability of IIF based on experimentally derived heuristic rules (Mazur, 1977). Pitt and Steponkus further developed Mazur's IIF model by incorporating statistical distributions of experimental variables (Pitt and Steponkus, 1989). Cravalho and colleagues were the first to develop a mechanistic thermodynamic model of the intracellular water-ice phase transition (Toscano, 1975). Subsequently, Toner adapted classical nucleation theory to the problem, resulting in a model which could successfully

predict the kinetics of IIF in the absence of cryoprotective chemical additives (Toner, *et al*., 1990). These modern models have been shown to be accurate for predicting the response of cell suspensions during the cryopreservation process (Toner, 1993), and their usefulness in computer-aided protocols has been demonstrated (Karlsson, *et al*. 1996). However, they are of limited value for the analysis of IIF in multicellular tissues and organs.

1.5 Modeling of Tissue Freezing

Early models of the response of tissues to freezing focused on transport processes, specifically the effects of gradients resulting from the macroscopic dimensions of these systems. For example, Levin *et al*. developed a model of water transport in a multi-layer cell cluster, demonstrating that the kinetics of cell dehydration were affected by the additional barriers to transport (Levin, *et al*. 1977). The effect of vasculature on cell dehydration was analyzed by Rubinsky using a Krogh cylinder model (Rubinsky, 1989), and the effects of the extracellular matrix on the water transport process was considered by Diller and Raymond (1990). The Krogh cylinder model was later adapted to incorporate predictions of IIF in liver tissue (Devireddy, *et al*., 1999). These early models of the tissue response focus primarily on macroscale transport processes, and neglect microscale phenomena such as cell-cell and cell-substrate interactions, which play a major role in IIF in tissues.

Preliminary observations that the probability of IIF in cells cultured in monolayers was higher than the probability of IIF in suspensions of the same cell type suggested that cell-cell interaction enhances IIF (Acker, *et al*., 1999). These findings led to the

hypothesis that ice propagates from cell to cell (Berger and Uhrik, 1996; Acker, *et al*., 2001). In 2002, intercellular ice propagation was conclusively shown to be a real phenomenon by analysis of IIF in micropatterned cell pairs (Irimia and Karlsson, 2002). As outlined and discussed by Irimia and Karlsson (2002), several mechanisms of intercellular ice propagation have been proposed in the literature, but not conclusively established. One theory is that lysosomal enzymes released by a cell ruptured due to IIF compromise the membranes of adjoining cells and allow ice to propagate (McGann, *et al*., 1972). Another mechanism proposed is the catalysis of ice nucleation within a supercooled cell by the presence of ice crystals in neighboring cells (Tsuruta, *et al*., 1998; Acker and McGann, 1998). Propagation of ice through gap-junctions is the mechanism most heavily supported (Berger and Uhrik, 1992; Berger and Uhrik, 1996; Acker, *et al*., 2001; Irimia and Karlsson, 2002). Ice is thought to either physically grow through the gap-junctions (Acker, *et al*., 2001), or to cause conformational changes in the connexin proteins, exposing domains which act as heterogeneous nucleation sites on the unfrozen side of the gap-junction (Irimia and Karlsson, 2002).

Mathematical models of intercellular ice formation in tissues have been limited by the computational complexity of the algorithms. For example, the Markov chain model developed by Irimia and Karlsson (2002) uses an ordinary differential equation to solve for the probabilities of each IIF state of the tissue. In this application, the number of possible IIF states is $\sim 2^{n_{cells}}$ where n_{cells} is the total number of cells in the tissue. Thus, due to the computational cost of such models, the maximum tissue size that can be modeled in practice is ~ 5 cells.

Another approach for modeling intercellular ice propagation in tissues has been the implementation of Monte Carlo techniques to determine location and time of freezing events within a construct (Irimia and Karlsson, 2002). An example of the freezing kinetics predicted by the Monte Carlo method for a tissue 20x20 cells in size can be seen in Figure 1.1. This technique is also limited by its computational complexity. As the algorithms of the Monte Carlo simulations are performed, the state of each cell in the tissue must be tracked, and the probability of individual IIF events in each cell calculated, causing the complexity to increase as $O\{n_{cells}^2\}$. The maximum tissue size that can be simulated using the Monte Carlo model is approximately $n_{cells} \sim 10^5$ which translates to a tissue size of 1-10 mm^2 in a biological sample. Tissues used for engineering applications can be much larger in size; thus, the usefulness of the Monte Carlo method to predict IIF in a broad range of realistic applications is limited.

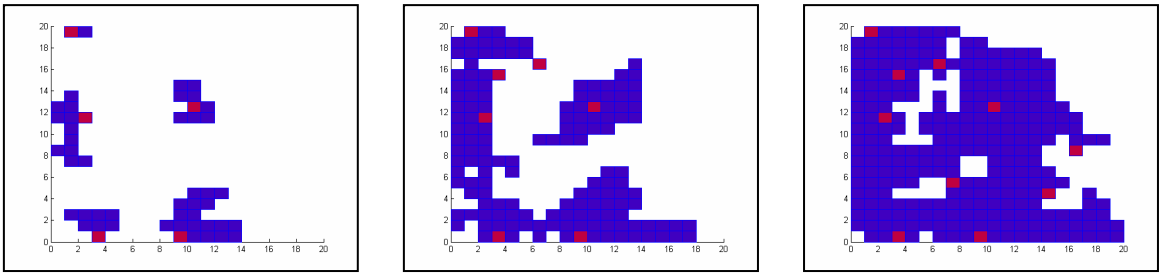

Figure 1.1. The progression of IIF in a 2-dimensional confluent tissue simulated using Monte Carlo techniques. Red indicates ice formation by nucleation. Blue indicates ice formation by propagation.

1.6 Scope of Present Work

The goal of the present work is to solve the problem of the prohibitive computational cost for prediction of IIF in macroscopic tissue constructs. This goal will be accomplished by the development of a model based on a continuum approximation of ice formation kinetics rather than using a model that relies upon iterative updating of the state of each cell individual cell within the tissue. The Johnson-Mehl-Avrami (JMA) model will be used as a framework for our continuum approximation, through identification of analogies between the microscale processes that govern the dynamics of tissue freezing and the nanoscale phenomena that characterize phase transformations in continuous media. Although the JMA model is formally applicable only to isothermal transformation kinetics, it is used here as an approximate description of IIF kinetics in tissues frozen under non-isothermal conditions. This approach is justified by imposing simplifying assumptions of the mechanisms of transformation, such that the corresponding kinetics become independent of temperature when expressed using non-dimensional variables.

First, the above approach will be applied to one-dimensional tissue constructs, resulting in the development of a modified 1-D JMA model for tissue freezing. This model will be validated by comparison to results of Monte Carlo simulations. Effects of finite tissue size will be analyzed using the Weinberg-Kapral theory for 1-D tissues. Similarly, a modified JMA theory will be developed for 2-D tissue constructs, and the model verified through comparison with Monte Carlo simulations of ice formation kinetics. Finally, predictions of the modified 2-D JMA model will be compared to experimental measurements of IIF kinetics in confluent monolayers.

CHAPTER 2

THEORETICAL BACKGROUND

2.1 Modeling of Intercellular Ice Propagation

Our model of IIF in confluent tissues is based on the theory of intercellular ice propagation developed by Irimia and Karlsson (2002). Thus, each cell in the tissue construct is assumed to admit only two IIF states, unfrozen and frozen. The average rate of IIF in an unfrozen cell is assumed equal to the sum of the rates associated with two independent stochastic processes: J_i, the average rate of spontaneous IIF by mechanisms independent of neighboring cell state (*e.g.*, intracellular ice nucleation); and J_p, the average rate of intercellular ice propagation across a cell-cell interface. In an unfrozen cell j with k_j frozen neighbors, the rate of IIF at time t can thus be expressed as

$$J_{IIF}^{j}(t) = J_i(t) + k_j \cdot J_p(t) \tag{2-1}$$

In actual biological systems, the nucleation and propagation rates may depend on time, position within the tissue, and the state of the cells in the construct. For one- and two-dimensional constructs, one can assume that all cells within the tissue experience the same conditions (*e.g.*, temperature and extracellular solute concentrations); therefore, spatial variations in J_i and J_p can be neglected. Following the original approach of Irimia and Karlsson (2002), a non-dimensional time is defined with respect to the rate of spontaneous IIF, as follows:

$$\tau \equiv \int_0^t J_i dt \tag{2-2}$$

With the above definition, the governing equations become independent of J_i, as a consequence of which the mechanism or time-dependence of this rate process does not

need to be known *a priori*. Furthermore, a non-dimensional intercellular propagation rate can be defined by the following expression

$$\alpha \equiv J_p / J_i \tag{2-3}$$

It has been shown that to a reasonable approximation, the non-dimensional propagation rate α can be assumed to be constant during non-isothermal freezing, if the rate of cooling is sufficiently fast that cell dehydration is negligible (Irimia and Karlsson, 2002). As a result, the equations governing the kinetics of IIF in tissue during non-isothermal freezing at rapid rates become temperature-independent when expressed in non-dimensional form. It is this observation which justifies the use of an isothermal transformation model (*i.e.*, the JMA model) to describe IIF under non-isothermal conditions.

In order to analyze the rate of growth of a cluster of frozen cells starting from an initial IIF event with $J_i = 0$ (*i.e.*, kinetics determined entirely from J_p), we will also define an alternative non-dimensional time variable:

$$\tau_p = \int_0^t J_p dt \tag{2-4}$$

The corresponding non-dimensional propagation rate will then take on a constant, unity value, independent of any temporal variations in J_p. With the present assumption of constant α, it is straightforward to convert between the two units of non-dimensional time, using the relationship

$$\tau_p = \alpha \tau \tag{2-5}$$

2.2 The Johnson-Mehl-Avrami Model of Transformation Kinetics

The classic Johnson-Mehl-Avrami (JMA) model describes the kinetics of isothermal transformation from a mother phase α to a daughter phase β, by nucleation (the process by which the formation of a new phase begins), growth, and impingement (the restriction of transformed region growth by other transformed regions). This model decouples the kinetics of nucleation and growth from the geometric constraints of impingement, greatly simplifying analysis of the problem.

The JMA theory is based on three main assumptions: an infinite volume V available for transformation, random nucleation, and growth of transformed regions without preference of direction. Specific simplifying assumptions have also been made about geometry and kinetics of nucleation and growth, in order to derive analytical solutions for special cases, such as zero-nucleation rate (pre-existing nuclei), constant nucleation rate, linear growth velocity, diffusion-limited growth, and growth of crystals in needle- or plate-like configurations (Christian 1975).

Several key concepts are defined in the classical development of the JMA model. Specifically, the "extended" volume is the total volume that would be transformed if growth of transformed regions were unimpeded by pre-existing transformed regions (*i.e.* neglecting impingement). The "phantom" volume is that part of the extended volume that overlaps previously transformed regions. In particular, phantom nuclei are those nuclei in the extended volume which appear in previously transformed regions.

For example, in Figure 2.1, the extended volume initially consists of A and B. During an infinitesimal time interval, the extended volume grows by transformation of the regions A', B', C, and D. The intersections A'$\cap$B and B'$\cap$A, as well as the nucleus D all represent phantom volumes, whereas these regions were already transformed. The nucleus D is a phantom nucleus.

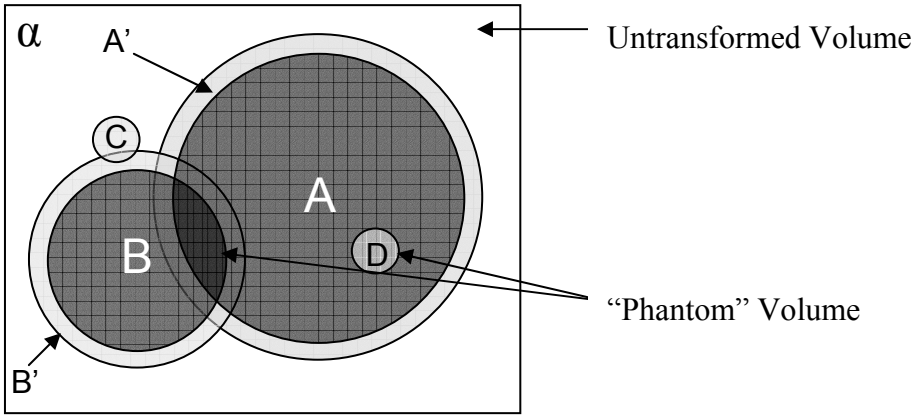

Figure 2.1. Schematic showing a 2-D phase transformation according to JMA theory. The spheres A and B represent regions of the transformed phase *β*, growing from the mother phase *α*. The shells A' and B' represent the hypothetical growth of A and B during an infinitesimal time interval, ignoring impingement. The spheres C and D represent nascent nuclei appearing during this time interval, neglecting impingement.

Below, the JMA model for a 1-D transformation with a constant nucleation rate and constant growth velocity is presented, following the derivation by Christian (1975). Neglecting impingment, the volume V_{t_n} at time t of a transformed region arising from a nucleation event at time t_n, is given by

$$V_{t_n}(t) = 2v(t - t_n) \tag{2-6}$$

assuming a constant growth rate v and neglecting the size of the initial nucleus. It follows that the contribution to the extended transformed volume, V_β^e, from all nucleation events in the time interval dt_n can be expressed as

$$dV_\beta^e = 2v(t - t_n)J_n V dt_n \tag{2-7}$$

where J_n is the average rate of nucleation per unit volume. Integrating over t_n gives the total extended volume

$$V_\beta^e(t) = \int_{t_n=0}^{t} 2v(t-t_n)J_n V dt_n \tag{2-8}$$

Defining the extended transformed volume fraction as $X_\beta^e \equiv V_\beta^e / V$, and assuming that the nucleation rate is constant, one obtains

$$X_\beta^e(t) = 2vJ_n t^2 \tag{2-9}$$

For many other assumed time dependencies for the nucleation rate and growth velocity, one obtains an expression for the extended transformed volume fraction of the general form

$$X_\beta^e(t) = kt^n \tag{2-10}$$

where k is known as the Avrami coefficient and n as the Avrami exponent (Christian 1975).

At some point of the transformation process, volumes from distinct domains of the transformed phase β throughout V will begin to impinge on each other and prevent further growth of those regions. The JMA theory accounts for this impingement effect to compute the actual transformed volume, V_β, from the extended volume fraction X_β^e. At any given time, t, the actual transformed volume fraction is $X_\beta \equiv V_\beta / V$, and the untransformed volume fraction is $(1 - X_\beta)$. During a subsequent time interval dt, the extended volume will increase by dV_β^e and the actual volume will increase by dV_β. Whereas the newly formed extended volume will be randomly distributed throughout V, the fraction of dV_β^e which will be phantom volume is X_β. Thus, only a fraction $(1 - X_\beta)$

of dV_β^e will be in untransformed material and contribute to the actual increase in transformed volume. Therefore,

$$dV_\beta = \left(1 - \frac{V_\beta}{V}\right) dV_\beta^e \tag{2-11}$$

Equation 2-11 can be integrated by separation of variables to yield the well-known Avrami transformation:

$$X_\beta = 1 - \exp\left(-X_\beta^e\right) \tag{2-12}$$

Substituting Equation 2-10 into Equation 2-12, one obtains the classical form of the JMA model:

$$X_\beta(t) = 1 - \exp(-kt^n) \tag{2-13}$$

While the JMA model has been shown to be widely applicable, there are many examples of cases where experimental data have not matched the predictions of the model (Erukhimovitch and Baram, 1994; Pusztai and Granasy, 1998; Clemente and Saleh, 2002; Srolovitz, *et al*., 1986; Van Siclen, 1996; Weinberg and Kapral, 1989; Tobin, 1974). In 1994, Erukhimovitch and Baram argued that this type of discrepancy was a result of the inclusion of phantom nuclei in the JMA model (Erukhimovitch and Baram, 1994). They proposed a modified JMA model excluding phantom nuclei from the calculation of transformation kinetics, and showed that the modified model more closely matched their experimental data (Erukhimovitch and Baram, 1994). However, the Erukhimovitch-Baram model was heavily criticized (Michaelsen, *et al*., 1996; Cahn, 1997b; Clemente and Saleh, 2002) and initiated a wave of responses in support of the

JMA model and the inclusion of phantom nuclei in calculations of the transformed fraction (Cahn, 1996; Van Siclen, 1996; Fanfoni, *et al*., 2002; Weinberg and Kapral, 1989; Yu and Lai, 1996; Pineda and Crespo, 1999; Sessa, *et al*., 1996). In addition, several authors have independently derived the results of the JMA model without making use of the concept of phantom volumes (Van Siclen, 1996; Yu and Lai, 1996; Markworth, 1984; Yu and Lai, 1995; Kolmogorov, 1937; Cahn 1997a).

Many authors have suggested possible causes for the observed discrepancies between the JMA model and experimental data, including non-linear growth of crystals (Van Siclen, 1996), non-random nucleation (Clement and Saleh, 2002), and effect of finite sample size (Weinberg and Kapral, 1989). In the end, the overwhelming consensus is that the JMA model is applicable as long as the basic assumptions of the model are met.

2.3 Adaptation of JMA model to IIF in Biological Tissues

The JMA theory has been successfully adapted to describe transformation kinetics for a number of diverse applications. The JMA model has classically been used to describe solidification of metals, alloys and ceramics. But this model has also been used to describe liquid-gas phase transformation kinetics, *e.g*. the formation of droplets in vapors (Tunitskii, 1941) and the formation of gas bubbles in liquids (Kashchiev and Firoozabadi, 1993). The JMA model has even been used to describe biological phenomena, such as the crystallization kinetics of fats (Foubert, *et al*. 2003). In the present work, we will adapt the JMA theory to describe the kinetics of IIF in biological tissues.

We will consider a tissue consisting of n_{cells} discrete cells, any of which may undergo IIF. The kinetics of IIF are typically quantified by calculating the cumulative fraction of IIF,

$$P_{IIF} \equiv \frac{n_{IIF}}{n_{cells}} \tag{2-14}$$

where n_{IIF} is the number of cells with intracellular ice. We now hypothesize that if the tissue is large ($n_{cells} >> 1$), it can be approximated as a continuum material, with the probability P_{IIF} becoming a continuous variable representing the transformed fraction, in analogy with X_β. Recalling that IIF in tissues occurs via spontaneous (interaction-independent) processes and by propagative processes among interacting cells, we identify spontaneous IIF as analogous to nucleation of the β phase, and intercellular ice propagation as analogous to the growth of the β phase. Similarly, the impingement effect described by the JMA theory is mirrored by the coalescence of distinct domains of frozen cells during the tissue freezing process.

Thus, our goal is to develop a modified JMA model to describe the kinetics of transformation events during the freezing of a confluent tissue construct. Below, a 1-D tissue will be considered, *i.e.* a linear chain of interacting cells, each of which is in contact with exactly two neighbors. The model is developed in analogy with the derivation of the classical JMA theory as summarized in Section 2.2. Thus, initially the growth of a single transformed domain in the absence of impingement is considered. The first IIF event must occur via an interaction-independent mechanism, such as intracellular nucleation. If this initial nucleation event occurs at time t_n, and is followed by

intercellular ice propagation at a rate J_p in both directions, then the number of frozen cells at time t will be

$$n_{t_n}(t) = 1 + 2 \cdot \int_{t_n}^{t} J_p(t') \cdot dt' \tag{2-15}$$

where t' is a dummy variable for integration. Rewriting Equation 2-15 in non-dimensional form using Equations 2-2 and 2-3, one obtains

$$n_{t_n}(\tau) = 1 + 2 \cdot \alpha \cdot (\tau - \tau_n) \tag{2-16}$$

where τ_n is the non-dimensional time corresponding to t_n. Next, an extended transformed fraction is defined as

$$P_{IIF}^{e} \equiv \frac{n_{IIF}^{e}}{n_{cells}} \tag{2-17}$$

where $n_{IIF}{}^{e}$ is the number of frozen cells in the tissue neglecting impingement (*i.e.,* allowing IIF to occur more than once in the same cell). The contribution to $n_{IIF}{}^{e}$ from the frozen domains initiated in the time interval dt_n is

$$dn_{IIF}^{e} = n_{t_n}(t) \cdot n_{cells} \cdot J_i \cdot dt_n \tag{2-18}$$

and converting to non-dimensional form. Substituting Equation 2-16 into Equation 2-18, one obtains

$$n_{IIF}^{e}(\tau) = n_{cells}\int_{0}^{\tau}\left[1 + 2\alpha\cdot(\tau - \tau_n)\right]\cdot d\tau_n \tag{2-19}$$

Thus, the extended transformed fraction is

$$P_{IIF}^{e} = \alpha\tau^2 + \tau \tag{2-20}$$

for IIF in 1-D tissue constructs with constant α. More generally, if the growth law $n_{t_n}(\tau)$ depends only on the difference τ-τ_n, then the extended transformed fraction is given by

$$P_{IIF}^{e}(\tau_p) = \frac{1}{\alpha}\int_{0}^{\tau_p} n_0(\tau_p)d\tau_p \tag{2-21}$$

where $n_0(\tau_p)$ is the number of frozen cells in a transformed domain which is nucleated at $t_n = 0$.

By analogy with the Avrami transformation (Equation 2-12), the cumulative probability of intracellular ice formation can be computed from the extended transformed fraction as follows:

$$P_{IIF} = 1 - \exp\left(-P_{IIF}^{e}\right) \tag{2-22}$$

In particular, for 1-D tissues with constant α,

$$P_{IIF} = 1 - \exp\left(-\alpha\tau^2 - \tau\right) \tag{2-23}$$

To further extend the analogy with the general JMA model (Equation 2-13), we hypothesize that the transformation kinetics of IIF in biological tissues can be described by the generalized model of the form

$$P_{IIF} = 1 - \exp\left\{-k\tau^n - \tau\right\} \tag{2-24}$$

for a wide range of tissue geometries and mechanisms of nucleation or intercellular ice propagation.

2.4 The Weinberg-Kapral Model of Transformation Kinetics

As previously discussed, the JMA model will not match experimental data if the assumptions of the model are not met. One assumption which is sometimes not applicable in practical uses is the availability of an infinite volume of untransformed material. To determine the effect of finite-size medium on the transformation kinetics, Weinberg and Kapral developed a probabilistic theory of phase transformation based on a model which was discretized in time and space (Weinberg and Kapral, 1989). With the exception of allowing for finite sample dimensions, the Weinberg-Kapral (WK) theory is based on the same assumptions as the JMA theory including random nucleation, but

provides a more accurate account of transformation kinetics in regions near the boundary of the sample.

Weinberg and Kapral define a non-dimensional discrete time $\bar{t}$ such that each time interval has unity magnitude, and a non-dimensional growth velocity *v* which is allowed to assume integral values only. They model the kinetics of transformation in a *d*-dimensional hyper-cubic lattice with a constant velocity *v* in the directions of each of the orthogonal axes of the lattice. Thus, the transformed region initiated from a single nucleation event is a *d*-dimensional hypercube, which will comprise $(2v\bar{t}+1)^d$ lattice sites at time $\bar{t}$ following the initial nucleation. Below, the results of Weinberg and Kapral will be derived for the cases of discrete nucleation (*i.e.*, pre-existing nuclei with no further nucleation during the transformation) and continuous nucleation (nucleation at a constant rate throughout the transformation).

2.4.1 Discrete Nucleation

Weinberg and Kapral initially consider the case of pre-existing nuclei, with no formation of additional nuclei during the transformation process. If the fraction of lattice sites which are transformed at time $\bar{t} = 0$ is *p*, then the transformed fraction in an infinite lattice is given by

$$X_\beta(\bar{t}) = 1-(1-p)^{(2v\bar{t}+1)^d} = 1-\exp\left[(2v\bar{t}+1)^d \cdot \ln|1-p|\right] \qquad (2\text{-}25)$$

Equation 2-25 was initially derived by Bradley (1987), and represents a JMA analogue for hyper-cubic growth of pre-existing nuclei on a discrete lattice.

The WK model considers a d-dimensional hyper-cubic region V_ξ bounded by two d-1 dimensional hyperplanes P_1 and P_2, such that the thickness in the remaining dimension is ξ. As shown in Figure 2.2, the volume can be divided into three distinct regions: if $v\bar{t} < (\xi\text{-}1)/2$, then there exists a central region C which is unaffected by the truncation of the lattice at P_1 and P_2; conversely, in the boundary layers B_1 and B_2, the kinetics of transformation will be slower than in C, due to edge effects. If $v\bar{t} \geq (\xi\text{-}1)/2$, then the transformation kinetics throughout the volume V_ξ will be affected by the finite dimensions of the lattice. However, in this case, if $v\bar{t} < \xi\text{-}1$, the kinetics of transformation in central region D will still be different from the transformation kinetics in boundary layers E_1 and E_2 (see Figure 2.2b)

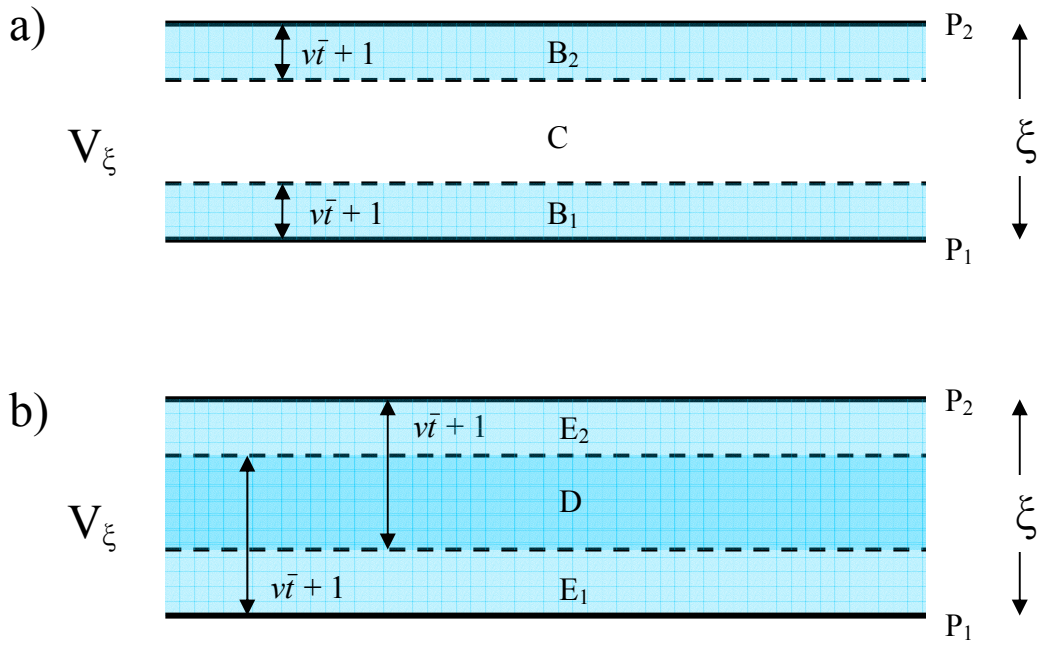

Figure 2.2. Schematic diagram of volume V_ξ, showing the boundary planes P_1 and P_2. (a) Boundary layers B_1 and B_2, and central region C, for $v\bar{t}$ < (ξ-1)/2. (b)Boundary layers E_1 and E_2, and central region D, for (ξ-1)/2 ≤ $v\bar{t}$ < (ξ-1), (Weinberg and Kapral, 1989).

For the initial stages of the transformation, *i.e.*, $v\bar{t}$ < (ξ-1)/2, the thickness of the boundary layers is $v\bar{t}$ +1. Whereas the central layer C is unaffected by edge effects, the kinetics of transformation within this region are identical to those for the case of an infinite lattice, *i.e.*, $X_c(\bar{t}) = X_\beta(\bar{t})$, where X_β is given by Equation 2-25, and X_c represents the transformed fraction in C.

To determine the fraction transformed in the boundary layers, a layer that is i units away from the lattice boundary (P_1 or P_2) is considered. The probability that a randomly chosen site in layer i is untransformed can be written as

$$Z_i(\bar{t}) = (1-p)^{(2v\bar{t}+1)^{d-1}(v\bar{t}+i)} \qquad \text{where} \quad (1 \le i \le v\bar{t}+1) \tag{2-26}$$

By summing over all the possible layers *i* within the boundary regions, the transformed volume fraction in layer B_1 is obtained,

$$X_{B_1}(\bar{t}) = \frac{1}{v\bar{t}+1}\sum_{i=1}^{v\bar{t}+1}\left[1-(1-p)^{(2v\bar{t}+1)^{d-1}(v\bar{t}+i)}\right] \tag{2-27}$$

By symmetry, $B_1(\bar{t}) = B_2(\bar{t})$, so the volume fraction for the entire region ξ is found by the following equation:

$$X_{\xi}(\bar{t}) = \frac{\left[\xi - 2(v\bar{t}+1)\right]}{\xi}\cdot X_c(\bar{t}) + \frac{2(v\bar{t}+1)}{\xi}\cdot X_{B_1}(\bar{t}) \qquad (0 \le v\bar{t} \le \xi/2\text{-}1) \tag{2-28}$$

where the limits on $v\bar{t}$ have been set under the assumption that ξ is even.

For the case illustrated in Figure 2.2b, where $\xi/2\text{-}1 < v\bar{t} < \xi\text{-}1$, the boundary layers B_1 and B_2 have overlapped to create new boundary regions E_1 and E_2. The probability of a lattice site within region *D* being untransformed is

$$Z_D(\bar{t}) = (1-p)^{(2v\bar{t}+1)^{d-1}\xi} \tag{2-29}$$

Therefore, the transformed volume fraction can be written as

$$X_{\xi}(\bar{t}) = \frac{\left[2(v\bar{t}+1)-\xi\right]}{\xi}\cdot\left[1-(1-p)^{(2v\bar{t}+1)^{d-1}\xi}\right] + \frac{2(v\bar{t}+1)}{\xi}\cdot X_{E_1}(\bar{t}) \quad (\xi/2\text{-}1 < v\bar{t} < \xi\text{-}1) \tag{2-30}$$

where

$$X_{E_1}(\bar{t}) = \frac{1}{v\bar{t}+1} \cdot \sum_{i=1}^{\xi-(v\bar{t}+1)} \left[1-(1-p)^{(2v\bar{t}+1)^{d-1}(v\bar{t}+i)}\right] \tag{2-31}$$

For the regime $v\bar{t} \geq \xi$-1, the original boundary layers B_1 and B_2 have spanned the entire width ξ, and the transformed volume fraction is given by

$$X_{\xi}(\bar{t}) = 1-(1-p)^{(2v\bar{t}+1)^{d-1}\xi} \qquad (v\bar{t} \geq \xi\text{-}1) \tag{2-32}$$

2.4.2 Continuous Nucleation

We will next consider the case of continuous nucleation, *i.e.*, there is a nonzero probability $r(\bar{t})$ of nucleation at each time step $\bar{t}$. In an infinite lattice, the probability that a randomly chosen site is untransformed at time $\bar{t}$ can be shown to be

$$Z(\bar{t}) = \prod_{i=0}^{\bar{t}} \left[1-r(i)\right]^{[2v(\bar{t}-i)+1]^d} \tag{2-33}$$

It follows that the transformed volume can be expressed as

$$X_{\beta}(\bar{t}) = 1-\prod_{i=0}^{\bar{t}} \left[1-r(i)\right]^{[2v(\bar{t}-i)+1]^d} \tag{2-34}$$

for an infinite-sized *d*-dimensional system with continuous nucleation and linear, hyper-cubic growth.

Weinberg and Kapral analyzed the effect of finite domain size on the kinetics of transformation by considering the case of continuous nucleation within the geometry illustrated in Figure 2.2. We note that Weinberg and Kapral considered $r(\bar{t})$ to be constant at all times, including $\bar{t} = 0$. However, whereas we wish to interpret $r(\bar{t})$ as the fraction of untransformed lattice sites which are transformed by nucleation (at constant rate) in the time interval between $\bar{t}$ -1 and $\bar{t}$, and since we will assume the nucleation and growth rates to be zero for $\bar{t} > 0$, we will set $r(0) = 0$, and $r(\bar{t}) = r$ for $\bar{t} > 0$, in contrast with the original derivation by Weinberg and Kapral (1989). With this exception, we followed the approach of Weinberg and Kapral, as summarized below. We also noted two typographical errors in the original paper, which are corrected here.

For calculation of the transformed fraction within the boundary layer B_1, the region is further subdivided as depicted in Figure 2.3. The boundary layer B_1 is divided into $\bar{t}$ strips labeled by the index ℓ, each of which contains v rows labeled by the index m. The boundary layer width is $v\bar{t}$ for convenience, rather than $v\bar{t} + 1$ as used in the discrete nucleation case.

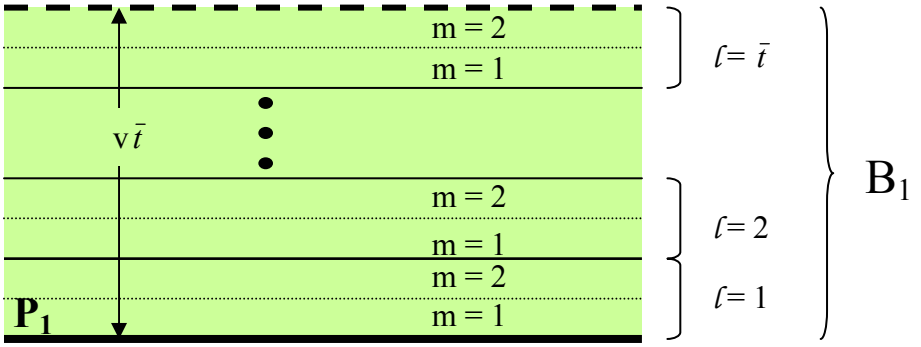

Figure 2.3. Enlargement of the B_1 region for the continuous seeding case (Weinberg and Kapral 1989). The region is divided into $\bar{t}$ strips labeled by ℓ, each of which contains v rows labeled by m. The case of $v = 2$ is shown.

Considering first the times for which $v\bar{t} < \xi/2$, the probability that a site in the m^{th} row of the l^{th} strip is not transformed as a result of any of the nucleation events at time $\bar{t}_i$ can be shown to be

$$Z_{l,m}(s_i) = \begin{cases} (1-r)^{(2vs_i+1)^d} & vs_i < (l\text{-}1)v + m \\ (1-r)^{(2vs_i+1)^{d-1}[vs_i+(l-1)v+m]} & vs_i \geq (l\text{-}1)v + m \end{cases} \quad (2\text{-}35)$$

where $s_i = \bar{t} - \bar{t}_i$, or the time available for growth of a site which nucleated at $\bar{t}_i$. The probability that a site within this row is untransformed at time $\bar{t}$ is thus the combined probability that no nucleation event in $0 \leq \bar{t}_i \leq \bar{t}$ (*i.e.*, $0 \leq s_i \leq \bar{t}$) caused transformation:

$$Z_{l,m}(\bar{t}) = \prod_{s_i=0}^{l-1}(1-r)^{(2vs_i+1)^d} \times \prod_{s_i=l}^{\bar{t}}(1-r)^{(2vs_i+1)^{d-1}[vs_i+(l-1)v+m]} \quad (2\text{-}36)$$

Equation 2-36 above, is the corrected version of Equation 4.6 from the original publication by Weinberg and Kapral (1989) which contains a typographical error (the numeral 1 was printed as a lowercase letter *l*).

Summing over all the rows *l* and *m* gives the total transformed volume fraction in region B_1:

$$X_{B_1}(\bar{t}) = 1 - \frac{1}{v\bar{t}} \sum_{l=1}^{\bar{t}} \sum_{m=1}^{v} Z_{l,m}(\bar{t}) \tag{2-37}$$

Noting again that the transformed fraction X_c has kinetics identical to those obtained in Equation 2-34 for the infinite lattice, the total volume fraction can be expressed as

$$X_{\xi}(\bar{t}) = \frac{\xi - 2v\bar{t}}{\xi} \cdot X_c(\bar{t}) + \frac{2v\bar{t}}{\xi} \cdot X_{B_1}(\bar{t}) \qquad (v\bar{t} \le \xi/2) \tag{2-38}$$

As in the discrete nucleation case, in the intermediate time regime ($\xi/2 \le v\bar{t} \le \xi$), the boundary layers B_1 and B_2 have grown to overlap, but have not yet crossed the entire width of the system. The formulation for $X_{E1}(\bar{t})$ is similar to that of $X_{B1}(\bar{t})$, but with different limits on the values of *l*

$$X_{E_1}(\bar{t}) = 1 - \frac{1}{\xi - v\bar{t}} \sum_{l=1}^{\xi/v - \bar{t}} \sum_{m=1}^{v} Z_{l,m}(\bar{t}) \tag{2-39}$$

The probability of transformation in the central region *D*, as a result of growth initiated by a given nucleation event, depends on the time at which nucleation occurred.

Thus the following expressions are obtained for the probability that a random site in the m^{th} row of the l^{th} strip is not transformed as a result of the nucleation events at time $\bar{t}_i$:

$$Z_{l,m}^{(1)}(s_i) = (1-r)^{(2vs_i+1)^d} \qquad \text{for} \quad (l\text{-}1)v + m > vs_i \qquad (2\text{-}40)$$

$$Z_{l,m}^{(2)}(s_i) = (1-r)^{(2vs_i+1)^{d-1}[vs_i+(l-1)v+m]} \qquad \text{for} \quad \xi\text{-}(l\text{-}1)v\text{-}m > vs_i \geq (l\text{-}1)v + m, \qquad (2\text{-}41)$$

$$Z_{l,m}^{(3)}(s_i) = (1-r)^{(2vs_i+1)^{d-1}\xi} \qquad \text{for} \quad vs_i \geq \xi\text{-}(l\text{-}1)v\text{-}m \qquad (2\text{-}42)$$

By taking the product of the above probabilities,

$$Z_{l,m}(\bar{t}) = \prod_{s_i=0}^{l-1} Z_{l,m}^{(1)}(s_i) \times \prod_{s_i=l}^{\xi/v-l} Z_{l,m}^{(2)}(s_i) \times \prod_{s_i=\xi/v-l+1}^{\bar{t}} Z_{l,m}^{(3)}(s_i) \qquad (2\text{-}43)$$

the probability of a site remaining untransformed at time $\bar{t}$ is found. The expression for $X_D(\bar{t})$ is calculated as follows:

$$X_D(\bar{t}) = 1 - \frac{1}{v\bar{t} - \xi/2} \cdot \sum_{l=\xi/v-\bar{t}+1}^{\xi/2v} \sum_{m=1}^{v} Z_{l,m}(\bar{t}) \qquad (2\text{-}44)$$

Equation 2-44 above is a corrected form of the original Equation 4.15 as published in the paper by Weinberg-Kapral (1989). The endpoints for the summation over *l* should be (ξ/v)- $\bar{t}$ +1 to $\xi/2v$ as shown above rather than 1 to $\bar{t}$ -$(\xi/2v)$, as misprinted in the original paper.

Combining the transformation kinetics for the areas E_1, E_2 and D, the transformed volume fraction can be written as

$$X_{\xi}(\bar{t}) = \frac{2(\xi - v\bar{t})}{\xi} X_{E_1}(\bar{t}) + \frac{(2v\bar{t} - \xi)}{\xi} X_D(\bar{t}) \quad \text{for} \quad \xi/2 \le v\bar{t} \le \xi \qquad (2\text{-}45)$$

Finally, for the case when $v\bar{t} > \xi$, the transformed volume fraction is given by

$$X_{\xi}(\bar{t}) = 1 - \frac{1}{\xi} \sum_{l=1}^{\xi/v} \sum_{m=1}^{v} Z_{l,m}(\bar{t}) \qquad \text{for} \quad v\bar{t} > \xi \qquad (2\text{-}46)$$

where $Z_{l,m}(\bar{t})$ is calculated using Equation 2-43.

2.4.3 Comparison of Weinberg-Kapral model with Monte Carlo Simulations

Because the dimensionless variables used by Weinberg and Kapral in Equations 2-25 to 2-46 are different from those used in our model of IIF (Equations 2-1 through 2-5), we must establish a relationship between the two sets of variables, in order to compare the predictions of the WK theory to our Monte Carlo predictions. To whit, the non-dimensional time used by Weinberg and Kapral was defined

$$\bar{t} \equiv t / \Delta t \qquad (2\text{-}47)$$

where Δt is an arbitrary time interval. Whereas the growth velocity v in the WK model represents the average number of lattice sites traversed by a transformation front in the time interval Δt, this quantity is related to our average propagation rate J_p as follows:

$$v = \int_{t-\Delta t}^{t} J_p \, dt \tag{2-48}$$

Similarly, the nucleation probability r in the WK model represents the probability of nucleation in the time interval Δt and is therefore related to our rate of spontaneous IIF, J_i, as follows:

$$r = 1 - \exp\left[- \int_{t-\Delta t}^{t} J_i \, dt \right] \tag{2-49}$$

To simplify the mathematics, we will assume, without loss of generality, that J_i and J_p are constant. Thus, Equation 2-4 becomes

$$\tau_p = J_p t \tag{2-50}$$

and Equations 2-48 and 2-49 simplify to

$$v = J_p \Delta t \tag{2-51}$$

$$r = 1 - \exp\left[-J_i \Delta t\right] \tag{2-52}$$

respectively. Combining Equations 2-47, 2-50, and 2-51, we obtain the identity

$$\bar{t} = \tau_p \tag{2-53}$$

Likewise, substitution of Equations 2-5 and 2-51 into Equation 2-52 yields

$$r = 1 - \exp\left[-\frac{v}{\alpha}\right] \tag{2-54}$$

In the WK model, the time step Δt is restricted such that the growth rate v will take integer values only. Thus, we will arbitrarily set $v = 1$. Thus, if $\alpha >> 1$, then Equation 2-54 can be approximated by

$$r = \frac{1}{\alpha} \tag{2-55}$$

Thus, to compare predictions of the WK model to our Monte Carlo simulations, we converted the relevant parameters using Equations 2-53 and 2-55, and evaluated the WK model using a unity magnitude growth velocity.

CHAPTER 3

METHODS

3.1 Monte Carlo Algorithms

3.1.1 Discrete Nucleation

To investigate the effect of intercellular ice propagation on the growth rate of transformed domains in the tissue, we simulated the kinetics of IIF in tissues resulting from discrete nucleation events occurring prior to the onset of growth. Thus, whereas the rate of spontaneous IIF (J_i) was assumed to be zero during the simulation, growth occurred only by intercellular ice propagation from one or more pre-existing IIF "nuclei". The IIF kinetics in 1- and 2-D tissues were simulated using previously developed Monte Carlo techniques (Irimia, 2002; Irimia and Karlsson, 2004) summarized below. The tissue structure was approximated as a regular linear square lattice in which each lattice site represented an individual cell. Cell-cell interactions via intercellular ice propagation were allowed only between nearest neighbors. In such a system, the probability that an unfrozen cell at lattice site j will freeze in a time interval Δt is described by a Poisson process,

$$p_{IIF}^{j}(\Delta t) = 1 - \exp\left\{ - \int_{t}^{t+\Delta t} J_{IIF}^{j}(t) \cdot dt \right\} \tag{3-1}$$

where $J^{j}_{IIF}(t)$ is given by Equation 2-1, with $J_i = 0$. Non-dimensionalizing the above equation using Equations 2-4, and assuming that the probability of IIF occurring in two

neighboring cells within the same time interval is negligible, one obtains a homogeneous Poisson process:

$$p_{IIF}^{j}(\Delta\tau_p) = 1 - \exp\{-k_j \Delta\tau_p\} \tag{3-2}$$

where $\Delta\tau_p \equiv \tau_p(t+\Delta t)-\tau_p(t)$. To enforce the validity of the assumption that k_j is constant during $\Delta\tau$, the probability of an IIF event occurring anywhere in the tissue during this time interval was required to be bounded by some small probability ε, resulting in the constraint

$$\Delta\tau_p \le \frac{-\ln\{1-\varepsilon\}}{\sum_j (k_j)} \tag{3-3}$$

where the sum is taken over all unfrozen cells in the tissue. For time intervals satisfying Equation 3-3, the probability of multiple IIF events occurring in the same neighborhood during the time interval $\Delta\tau_p$ is much smaller than ε. Furthermore, Equation 3-2 can be linearized, as follows

$$p_{IIF}^{j}(\Delta\tau_p) \approx k_j \Delta\tau_p \tag{3-4}$$

Simplifying Equation 3-3 by noting that ε is a lower bound for the expression $-\ln(1-\varepsilon)$, we interatively updated the state of our simulated tissue at variable time intervals

$$\Delta\tau_p = \frac{\varepsilon}{\sum_j k_j} \tag{3-5}$$

After each time step $\Delta\tau_p$, a random number r_j was drawn from a uniform distribution on the interval (0,1), for every unfrozen cell j. An IIF event was recorded for cell j at the new time point if $r_j < p^j_{IIF}$, as calculated using Equation 3-4.

3.1.2 Continuous Nucleation

To simulate IIF with continuous nucleation at a rate $J_i > 0$, we adapted an algorithm originally developed by Gillespie for numerically simulating the stochastic time evolution of coupled chemical reactions (Gillespie, 1976); this Monte Carlo algorithm is more accurate and efficient than the one outlined in Section 3.1.1 for large tissues. To adapt Gillespie's algorithm to our problem, we represented each IIF event as a "reaction", the conversion of a cell j from its unfrozen to its frozen state. Thus, the state of each cell j was described by a variable h_j, defined as follows

$$h_j(\tau) = \begin{cases} 1 & \text{if cell } j \text{ is unfrozen at time } \tau \\ 0 & \text{if cell } j \text{ is frozen at time } \tau \end{cases} \tag{3-6}$$

The conversion of an unfrozen cell j can occur via spontaneous IIF at a rate J_i, or via propagation from any frozen nearest neighbors, at a rate J_p, as shown in Figure 3.1. Using Equations 2-1 and 2-2, one can thus write a non-dimensional rate of conversion of the unfrozen cell j:

$$c_j(\tau) = 1 + k_j(\tau) \cdot \alpha \tag{3-7}$$

The overall rate of IIF in the tissue at time τ, in non-dimensional units, is therefore

$$a_o(\tau) = \sum_{j=1}^{n_{cells}} h_j(\tau) c_j(\tau) \tag{3-8}$$

where n_{cells} is the total number of cells in the tissue.

Gillespie defined a *reaction probability density function*

$$\mathrm{P}(\delta\tau, j) = h_j c_j \cdot e^{-a_0 \cdot \delta\tau} \tag{3-9}$$

which is a joint probability density function on the discrete variable *j*, representing the next reaction (IIF event) which will occur, and the continuous variable δτ, representing the time until the occurrence of this IIF event in cell *j*. To generate a pair of random variables (δτ,*j*) according to the joint probability function defined by Equation 3-9, one begins by drawing two random numbers r_1 and r_2, uniformly distributed on the interval [0,1] (Gillespie, 1976). To obtain the time interval until the next reaction, one transforms r_1 as follows:

$$\delta\tau = \frac{1}{a_0} \cdot \ln\left(\frac{1}{r_1}\right) \tag{3-10}$$

To determine which cell *j* is converted to the frozen state, one finds the value of *j* which satisfies the inequality

$$\frac{1}{a_0}\sum_{m=1}^{j-1} h_m c_m < r_2 \le \frac{1}{a_0}\sum_{m=1}^{j} h_m c_m \tag{3-11}$$

Our Monte Carlo algorithm thus started at $\tau = 0$, computed $\delta\tau$ using Equation 3-10, and updated the non-dimensional time variable by this amount. An IIF event was recorded for cell *j* at this new time point, where the index *j* had been determined using Equation 3-11. After updating the state of the tissue, this process was repeated with a new pair of random numbers.

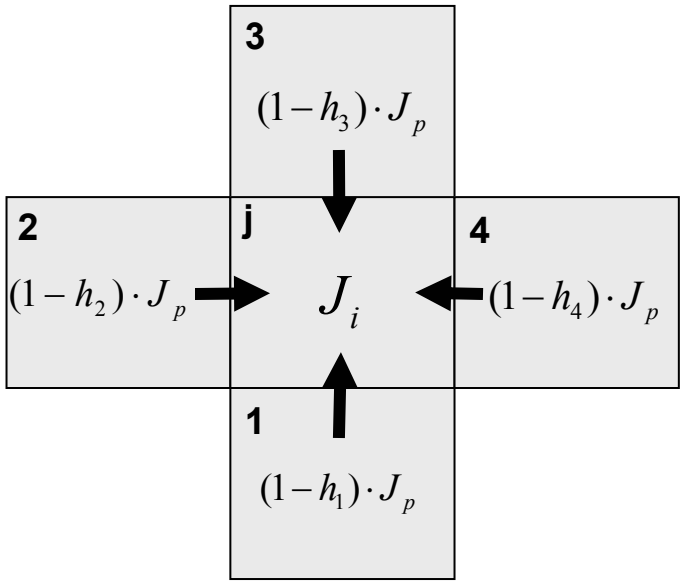

Figure 3.1. A schematic of the IIF kinetics simulated by the Gillespie algorithm. Unfrozen cell *j*, which is surrounded by four neighbors, can be converted to a frozen state via spontaneous IIF at a rate J_i, or via intercellular ice propagation from adjoining cells, at the indicated rate. See text for definition of variables.

3.2 Experimental Materials and Methods

3.2.1 Cell Culture

As previously described by Irimia and Karlsson (2002), the human hepatoma cell line HepG2 (American Type Culture Collection, Manassas, VA) was cultured at 37˚C under a humidified 5% CO_2 atmosphere in minimum essential medium (MEM; Gibco BRL Life Technologies, Gaithersburg, MD) supplemented with 10% (v/v) fetal bovine serum (FBS; Sigma, St. Louis, MO), 2.2 g/L sodium bicarbonate (Sigma-Aldrich, St. Louis, MO), 1 mM sodium pyruvate (Sigma), 100 μg/ml streptomycin (Roche Molecular Biochemicals, Indianapolis, IN), and 100 U/ml penicillin (Roche Molecular Biochemicals). Media were replaced every two days, and subcultivation occurred once a week by washing in Ca^{+2} and Mg^{+2} free Dulbecco's Phosphate Buffered Solution (PBS; Gibco), disaggregation in a solution of 0.2% w/v trypsin (Gibco), 0.2% w/v glucose (Sigma), and 0.5 mM EDTA (Sigma) in PBS, followed by a resuspension in culture medium and replating at a ratio of 1:5.

3.2.2 Sample Preparation

For preparation of monolayer cultures for cryomicroscopy experiments, cells were trypsinized as described above, suspended in cell culture medium, and washed by centrifugation for 2.5 minutes at 200 x *g*. The supernatant medium was aspirated, and cells resuspended in a versene solution consisting of 5 mM EDTA in PBS to chelate Ca^{+2} and prevent cell-cell aggregation. The cells were once again centrifuged for 2.5 minutes at 200 x *g* and resuspended in culture medium. This suspension was then used to seed 16 mm circular coverslips which had been placed in 35 mm Petri dishes. Each Petri dish

was seeded using a 2 ml suspension of cells at a density of ~0.65 X 10^6 cells / ml. Following a one-hour incubation under culture conditions, the medium was aspirated from the Petri dishes, the coverslips washed with PBS, and the medium replaced. The coverslips were then returned to culture for approximately 7 days, until a confluent monolayer had formed.

After cells had grown to a confluent monolayer on the coverslip, the medium was aspirated and the coverslip incubated at 37˚C for 15 minutes in 2 μM SYTO-13 (Molecular Probes, Eugene, OR) in PBS. This fluorescent dye stains nucleic acid and thus allowed for the visualization of nuclei, which aided in the quantification of the number of cells in the monolayer. Cryomicroscopy experiments required that the cell monlayer be sealed between two coverslips. Thus, a clean coverslip was dotted with a fine ring of silicon grease (Dow Corning, Midland, MI) to provide a waterproof barrier, and 20 μl of the staining solution were dispensed into the center of this ring. The coverslip containing the monolayer of cells was then inverted on the other coverslip, forming a sandwich. All samples were used for microscopy immediately after preparation.

3.2.3 Cryomicroscopy

A cryomicroscopy system consisting of an Eclipse ME600 microscope (Nikon, Kanagawa, Japan) and a temperature-controlled microscope stage (FDCS 196; Linkam Scientific Instruments, Waterfield, Tadworth, Surrey, UK) was used to visualize the ice formation within the confluent monolayer. The temperature in the cryomicroscope stage was controlled by a feedback system (TMS 94; Linkam) and a liquid nitrogen pump

(LNP 94/2; Linkam) which were regulated by a Linksys32 software package (Version 1.1.1; Linkam). Experiments were recorded at 50 frames per second using a UNIQ UP-1830 digital camera (Uniq Vision, Inc., Santa Clara, CA) and the QED imaging software (Version 1.7.33; QED Imaging, Inc., Pittsburgh, PA).

Samples were placed into the chamber of the cryomicroscope, which was then sealed, and purged with dry nitrogen gas in order to remove water vapor. The samples were then cooled from 37˚C to -1.8˚C and ice seeded in the extracellular fluid by contacting the edge of the sample coverslip with a small silver block which had been chilled using liquid nitrogen vapor. The number of cells in the field of view was counted under epifluorescent illumination, prior to freezing. The sample was then cooled to -60˚C at a rate of 130˚C/min, with digital video images simultaneously acquired using a 50X objective and brightfield illumination. The intracellular freezing events manifested as a sudden darkening of the cytoplasm in the cells due to the scattering of the transilluminating light (Rall, *et al*., 1983). The cumulative incidence of IIF was determined by counting the number of frozen cells in each video frame, and by correlating the time of image acquisition with the recorded time-temperature data for the corresponding freezing experiment.

CHAPTER 4

TRANSFORMATION IN 1-D TISSUES

4.1 Introduction

The kinetics of transformations in 1-D tissues were initially analyzed, inasmuch as transformation in 1-D is less complex than in multi-dimensional systems, which permitted the development of a simple analytical solution using the JMA approach. The use of the JMA model as a continuum approximation of transformations in tissues consisting of discrete cells was validated by comparison of our 1-D modified JMA model to results of Monte Carlo simulations. Differences between the Monte Carlo and JMA models for small tissue sizes were attributed to edge effects resulting from the finite dimensions of the system, and the Weinberg-Kapral adaptation of JMA theory for finite-sized systems was used to accurately predict IIF in small tissues (Weinberg and Kapral, 1989). The effectiveness of the JMA model and its variations for predicting IIF in 1-D tissues under various conditions will be evaluated in this chapter.

4.2 The JMA model for 1-D Tissues

The use of the Johnson-Mehl-Avrami model to predict IIF in tissues was validated by comparison to Monte Carlo simulations of freezing in 1-D tissues. Monte Carlo simulations were performed using the Gillespie algorithm described in Section 3.1.2, with various values of non-dimensional ice propagation rate (α) and tissue size (n_{cells}). The

modified 1-D JMA model in Equation 2-23 was used to obtain theoretical predictions of IIF kinetics for comparison with the corresponding Monte Carlo simulations.

Monte Carlo simulations of freezing in large 1-D tissue constructs were compared to the modified 1-D JMA model for validation of the use of the JMA model as a continuum approximation of freezing in tissues. The number of cells in each tissue was $n_{cells} = 1500$, and non-dimensional propagation rate α was varied from 0.1 to 10^5. The simulations were performed for an ensemble of 200 tissue constructs for each value of α. As seen in Figure 4.1, individual freezing events at the beginning of the transformations did not conform to the expected linear trend because the initial freezing events for each tissue were randomly distributed, due to the stochastic nature of the process. As the transformations proceeded, the kinetics of the simulated IIF process converged to produce a linear trend in the Avrami plot, as expected. Freezing events near the end of the transformation again became random, resulting in non-linear trends in the final portion of the Avrami plots; consequently, the last 100 data points (< 0.03% of the data set) from each data set were discarded and are not shown in Figure 4.1. The theoretical predictions shown in Figure 4.1 are *a priori* predictions using Equation 2-23 with α values equal to those used for the corresponding Monte Carlo simulations. As expected, transformations occur faster for larger values of α. For values of $\alpha > 1$, predictions from the modified 1-D JMA model were in excellent agreement with results from the Monte Carlo simulations. For values of $\alpha \leq 1$, however, the modified 1-D JMA model was somewhat less accurate in predicting the kinetics obtained from the Monte Carlo simulations. This discrepancy at small α is expected. Because the equation parameter k is dependent on α, the first term in the expression of the extended P_{IIF} (Equation 2-24)

decreases rapidly for small α values. Whereas the linear term τ is subtracted from the extended transformed fraction in generating the Avrami plot for our model, only the power law term is included in our analysis. For small α, the kinetics of IIF are governed by the nucleation process represented by the linear term, and the signal-to-noise ratio in the power law term becomes smaller, providing unreliable results.

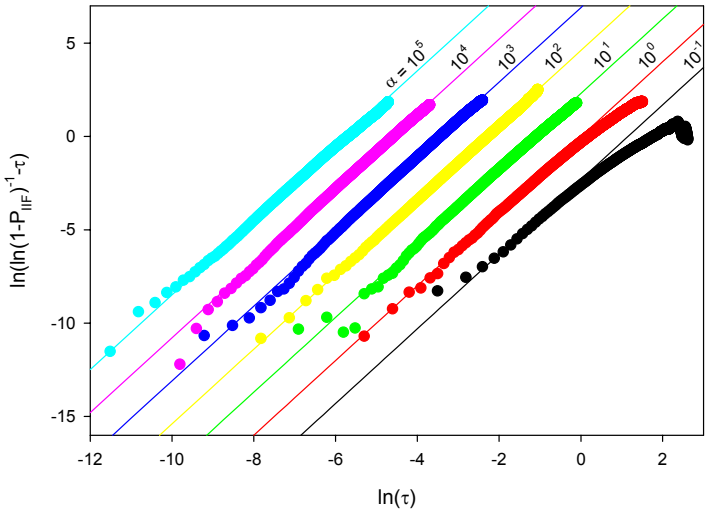

Figure 4.1. Comparison of Monte Carlo simulations (symbols) to predictions of the modified 1-D JMA model (lines) for various α values as indicated.

To determine the accuracy of the match of the modified 1-D JMA equation to the Monte Carlo model, simulation data described above was fit to the general modified JMA equation (Equation 2-24). The logarithmic transformation of the simulation data, excluding the last 100 points, was linearly curve-fit with R^2 values > 0.99 for $\alpha \geq 1$ and $R^2 = 0.93$ for $\alpha = 0.1$. The best-fit values for k were approximately equal to the expected

analytical values of $k = \alpha$ for all values of α considered (Figure 4.2). The best-fit values for n matched expected analytical values of $n = 2$ for $\alpha > 1$. As previously mentioned, the discrepancy between the Monte Carlo and JMA predictions for lower α values is a result of "noise" produced in the logarithmic transformation.

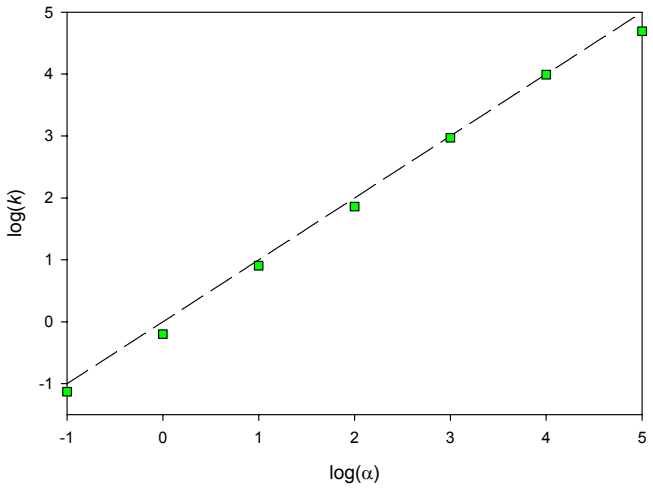

Figure 4.2. Avrami coefficient, k, obtained by curve-fitting results of the Monte Carlo simulations of 1-D tissue constructs (symbols) to the general modified JMA model. The theoretical predictions of $k = \alpha$ (dashed line) were obtained from Equation 2-23.

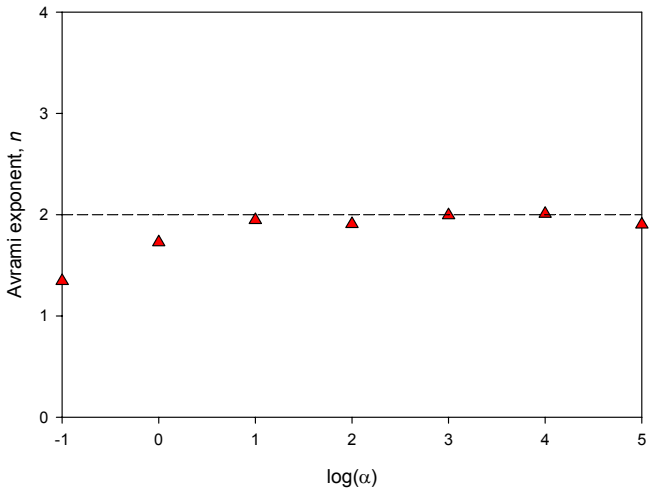

Figure 4.3. Avrami exponent, *n*, obtained by curve-fitting results of the Monte Carlo simulations of 1-D tissue constructs (symbols) to the general modified JMA model. The theoretical predictions of *n* = 2 (dashed line) were obtained from Equation 2-23.

Because the modified 1-D JMA model accurately predicted IIF in large tissues, a comparison of the modified 1-D JMA model was made to the Monte Carlo model for smaller-sized tissues. Monte Carlo simulations were performed for an ensemble of 1000 tissues consisting of 25, 50, 100, and 1000 cells in size with α = 1000. As seen in Figure 4.4, simulation data matched the modified 1-D JMA model when the number of cells in the tissue was equal to 1000. The difference between the modified 1-D JMA model and the Monte Carlo model increased as the tissue size decreased. This result was the first indication of the influence of tissue size in prediction of IIF by the Monte Carlo model, and demonstrated the need for an appropriate theoretical model for small tissue sizes.

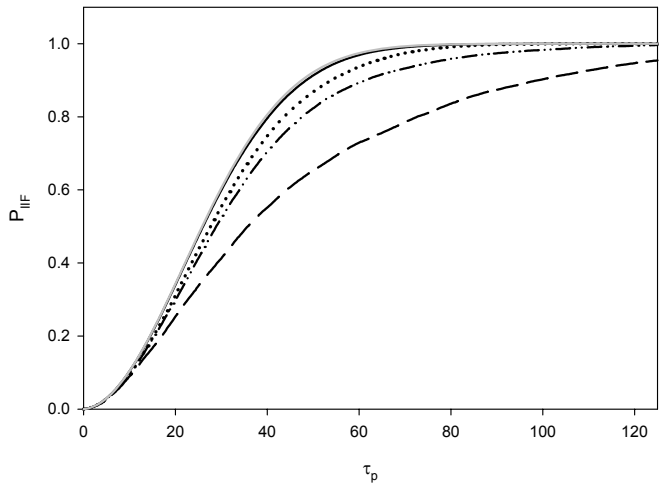

Figure 4.4. Comparison of Monte Carlo simulations (black lines) to the predictions of the modified 1-D JMA model (solid gray line). Monte Carlo simulations were performed for tissues consisting of 25 (long dash), 50 (dash-dot), 100 (dot), and 1000 (solid) cells with α = 1000.

4.3 The Weinberg-Kapral model for 1-D Tissues

As shown in Figure 4.4, tissue size greatly affects the transformation kinetics in tissue constructs, and a model to predict such kinetics in small tissues was needed. Because the Weinberg-Kapral model, discussed in Chapter 2, addresses the issue of boundary effects on transformations described by the JMA model, and because the Weinberg-Kapral variables could be easily adapted to those of the Monte Carlo model, the WK model was modified and implemented for comparison to Monte Carlo model predictions of IIF.

For the zero nucleation rate (discrete nucleation) case, Monte Carlo simulations were performed with the algorithm described in Section 3.1.1. The JMA model for discrete nucleation in a lattice described by Weinberg and Kapral (Equation 2-25) was used as the representative JMA model. The WK predictions were found using the model for discrete nucleation described in Section 2.4.1 with initial seeding density $p = 0.005$ or $p = 0.1$ and the tissue size $n_{cells} = 100$ or $n_{cells} = 1000$. Monte Carlo simulations were performed for an ensemble of 1000 tissues. In Figure 4.5, a comparison of results of the Monte Carlo simulations to the WK model and the discrete nucleation JMA model are shown. While the JMA model failed to match the predictions of the Monte Carlo model when $p = 0.005$, the WK model correctly predicted the transformed fraction in both tissue sizes. For the case when $p = 0.1$, the WK model more closely matched predictions of the Monte Carlo model than the JMA model for tissues 100 cells in size. Differences among all three models were negligible when $n_{cells} = 1000$.

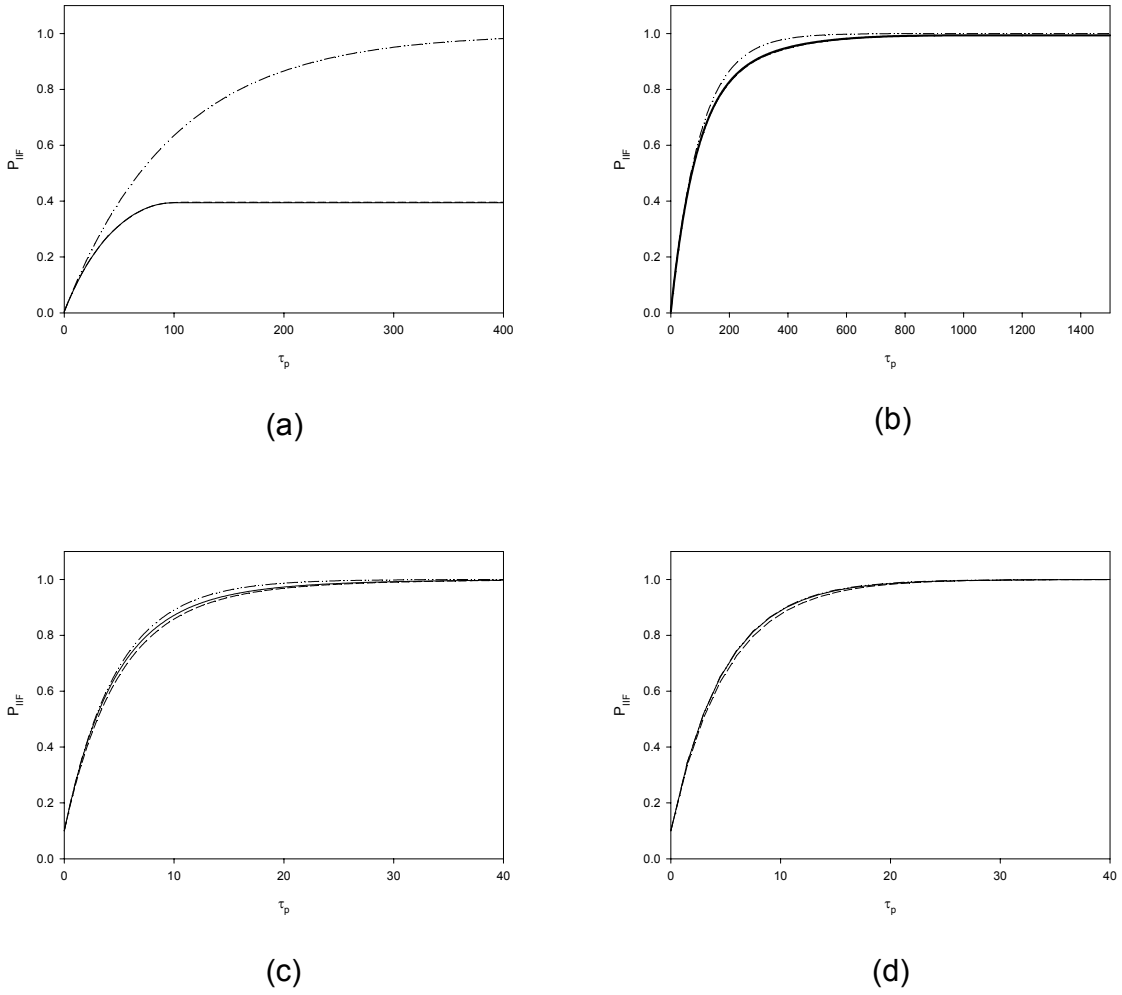

Figure 4.5. Comparison of Monte Carlo simulations (dashed line) to predictions of the discrete nucleation JMA model (dash-dotted line) and WK model (solid line), for p = 0.005 (a, b) or p = 0.1 (c, d) in tissues with n_{cells} = 100 (a, c) or n_{cells} = 1000 (b, d).

Next, the case of continuous nucleation in 1-D tissues was considered. Monte Carlo simulations were performed using the method described in Section 3.1.2 for various values of α and n_{cells}. The WK model for continuous nucleation described in Section

2.4.2 was used with values of α and n_{cells} corresponding to the Monte Carlo simulations. Two different JMA models were used for comparison. In Figure 4.6, Equation 2-34 (lattice JMA model for continuous seeding) described by Weinberg and Kapral and modified by setting $r(0) = 0$ was used for comparison. In Figure 4.8, Equation 2-23 (modified 1-D JMA model) developed in Section 2.3. Differences between these two JMA models were found to be negligible (graph not shown).

Mirroring the analysis presented in Figure 4.5, Monte Carlo simulations of tissue freezing with continuous nucleation were compared to the WK and JMA models. Monte Carlo simulations were performed for an ensemble of 1000 tissues with $n_{cells} = 100$ and $n_{cells} = 1000$ and with $\alpha = 100$ and 1000. These simulations were then compared to the WK model for continuous seeding and to the lattice JMA model for continuous seeding for the same conditions (Figure 4.6). The WK model for continuous seeding was identical to the lattice JMA model for continuous seeding, as expected, for large tissue size ($n_{cells} = 1000$), and correctly predicted the simulated P_{IIF} data for $\alpha = 1000$ (Figure 4.6d). In tissues with 100 cells, the Monte Carlo simulation data were divergent from the JMA model due to the size effect, but was predicted perfectly by the WK model (Figure 4.6 a, c).

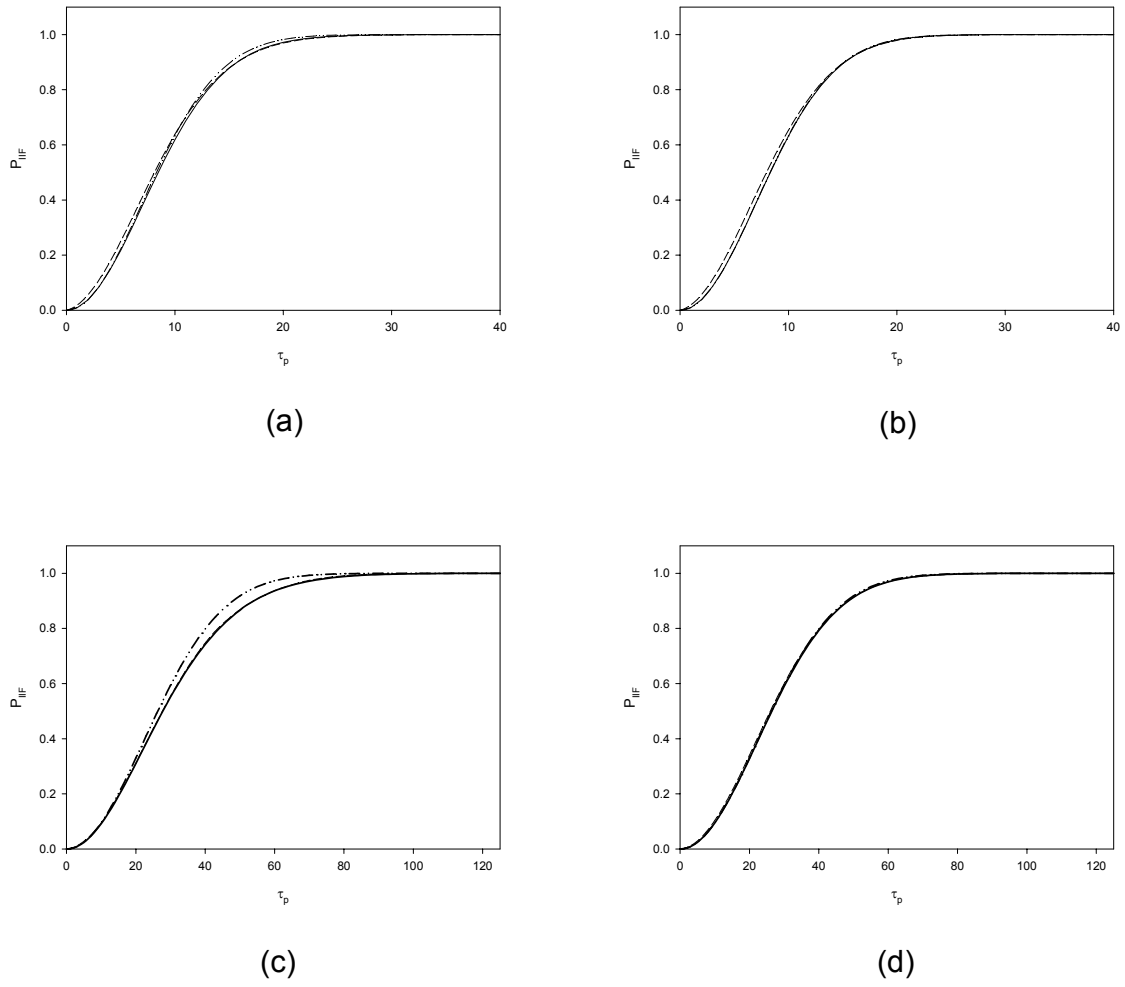

Figure 4.6. Comparison of Monte Carlo simulations (dashed line) to predictions of the lattice JMA model for continuous seeding (dash-dotted line) and the WK model (solid line), for $\alpha = 100$ (a, b) or $\alpha = 1000$ (c, d) in 1-D tissues with $n_{cells} = 100$ (a, c) or $n_{cells} = 1000$ (b, d).

To better show the accuracy of the WK model in predicting P_{IIF} for continuous seeding in 1-D tissues, a χ^2-test was performed on the difference between Monte Carlo simulation data and the WK model with χ^2 defined as follows:

$$\chi^2 = \frac{\sum_{i=1}^{N} \left[\left(P_{IIF}^{WK} \right)_i - \left(P_{IIF}^{MC} \right)_i \right]^2}{N} \qquad (4\text{-}1)$$

where N is the total number of simulation points considered, $(P_{IIF}{}^{MC})_i$ and $(P_{IIF}{}^{WK})_i$ correspond to the Monte Carlo and Weinberg-Kapral model predictions, respectively, at point i. Data points i corresponded to unit increments from time points $\tau_p = 0$ to $\tau_{p,final}$, where $\tau_{p,final}$ was the predicted time to reach complete transformation for each model rounded to the nearest integer. Simulations were performed for tissues of size = 2, 10, 100, and 1000 cells with α = 10, 100, 1000, and 10000. Monte Carlo models were based on $3x10^5$ tissues consisting of two cells, $1x10^4$ tissues consisting of 10 cells, 5000 tissues consisting of 100 cells, and 1000 tissues consisting of 1000 cells. From Figure 4.7, the trend is apparent that as α increases, the χ^2 value decreases for constant n_{cells}. This effect is due in part to the way the variables in the WK model are defined. Because the WK model assumes a seeding probability $r << 1$, and because r is related to the Monte Carlo model as $\alpha = r^{-1}$, the margin of error in the WK model increases as α decreases.

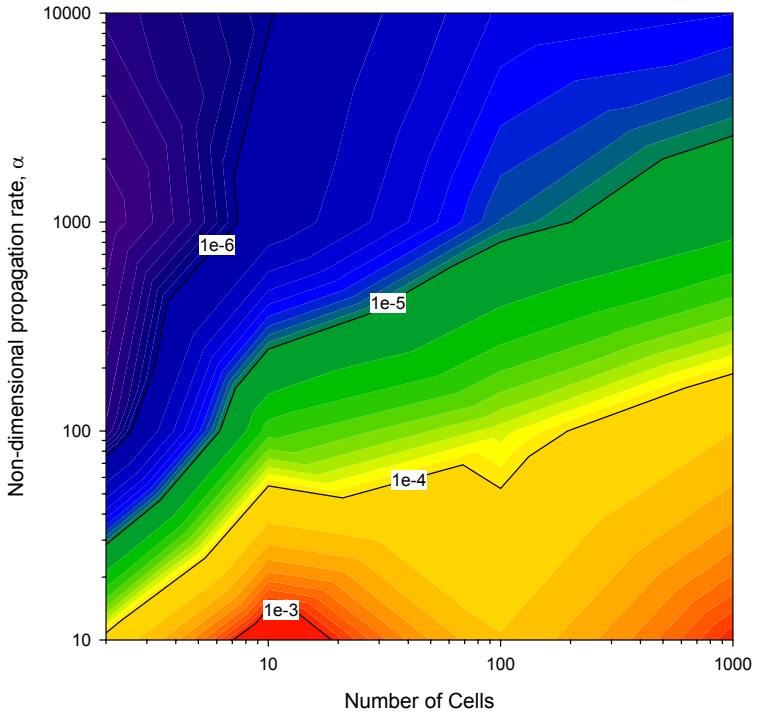

Figure 4.7. χ^2 comparison of the WK model to the Monte Carlo model of 1-D tissues with n_{cells} = 2, 10, 100, or 1000 with α = 10, 10^2, 10^3, 10^4.

The finite-size effect has been shown to play a large role in the progression of the transformation of a tissue, as seen in Figures 4.5-4.6. However, the precise conditions under which the transformation would be influenced of the size-effect were not clear. To determine the parameter conditions under which simulation data would exhibit no size effect, the WK model was compared to the modified 1-D JMA model by a χ^2-test (Figure 4.8). For this comparison, χ^2 was defined as follows:

$$\chi^2 = \frac{\sum_{i=1}^{N}\left[\left(P_{IIF}^{JMA}\right)_i - \left(P_{IIF}^{WK}\right)_i\right]^2}{N} \qquad (4\text{-}2)$$

where N is the total number of simulation points considered, $(P_{IIF}{}^{JMA})_i$ and $(P_{IIF}{}^{WK})_i$ correspond to the 1-D modified JMA equation predictions and Weinberg-Kapral model

predictions, respectively, at point *i*. Data points *i* corresponded to unit increments from time points $\tau_p = 0$ to $\tau_{p,final}$, where $\tau_{p,final}$ was the predicted time to reach complete transformation for each model rounded to the nearest integer. As expected, as tissue size increased, the difference between the WK and the JMA model decreased. Also, larger α values caused more size effect because clusters experienced faster growth that was more influenced by the boundaries than clusters in simulations with lower α values. Based on visual inspection of plots of simulation data and the modified 1-D JMA model (graphs not shown), parameter conditions below the line indicated in Figure 4.8 were found to yield negligible size-effects. Thus, the modified 1-D JMA model accurately describes the ice formation kinetics in 1-D tissues of an adequate size.

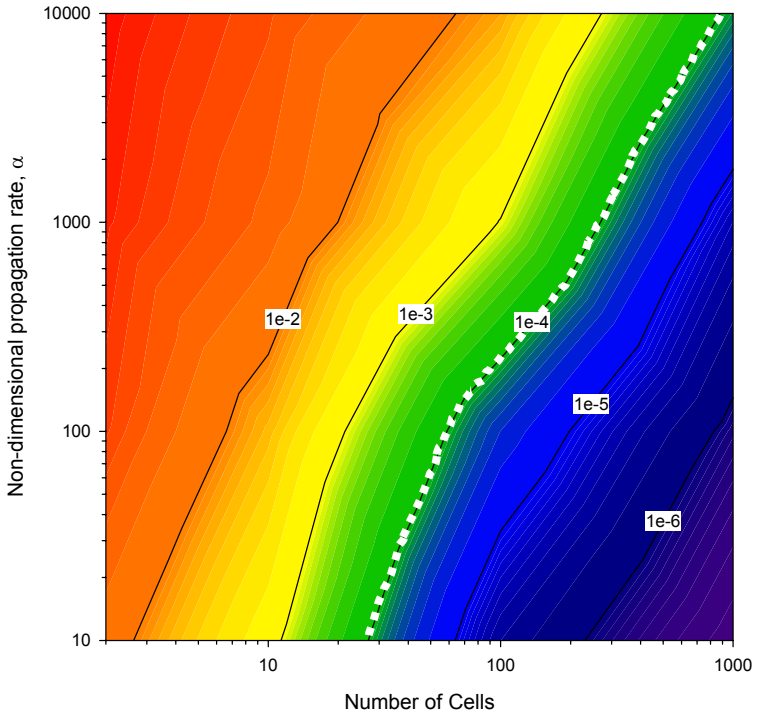

Figure 4.8. χ^2 comparison of WK model for continuous seeding to the modified 1-D JMA model for tissues with n_{cells} = 2, 10, 100, or 1000 with α = 10, 10^2, 10^3, 10^4. The white dotted line shows the region below which size-effects were negligible.

The results of the present chapter demonstrate that the modified 1-D JMA theory provides an accurate continuum approximation of transformation kinetics in 1-D tissue constructs of adequate size. For smaller tissue sizes, the Weinberg-Kapral model can be implemented to accurately predict IIF.

CHAPTER 5

TRANSFORMATION IN 2-D TISSUES

5.1 Introduction

In contrast with 1-D transformation kinetics, analysis of the kinetics of transformation in 2-D tissues proved more difficult due to the complexity of the growth rate in 2-D lattices. Whereas early attempts to develop an analytical JMA-type model produced poor results, we turned to phenomenological approaches based on numerical simulation of the growth process in 2-D tissues. Monte Carlo simulations of nucleation and growth indicated that size effects due to the finite computational domain were significant. Preliminary cryomicroscopy experiments were undertaken to measure the kinetics of IIF in monolayers of HepG2 cells, and these data were analyzed in the context of our theoretical and numerical models of transformation kinetics.

5.2 JMA Models of IIF Kinetics in 2-D Tissues

Several attempts were made to develop a JMA model to describe the kinetics of IIF in a 2-D tissue. All models assumed that transformation occurred in an infinite medium, and that the Avrami transformation for IIF (Equation 2-22) was valid. The growth kinetics of a single cluster, described by the function $n_0(\tau_p)$, were derived subject to various assumptions. These growth laws were integrated as shown in Equation 2-21 to yield the extended transformed fraction; the kinetics of IIF could then be obtained by applying the Avrami transformation (Equation 2-22).

5.2.1 Square Geometry with Constant Growth Velocity

We first used the constant-velocity growth law for 2-D transformation derived from the results of Weinberg and Kapral (1989) for growth of square domains, with a constant growth rate and concomitant continuous nucleation. Setting $d = 2$, $v = 1$, and converting the remaining variables using Equations 2-53 and 2-54, one obtains the extended transformed fraction

$$P_{IIF}^{e} = \frac{4}{3\alpha}\tau_p^{\,3} - \frac{1}{3\alpha}\tau_p \tag{5-1}$$

Monte Carlo simulations of IIF in an ensemble of 40 tissue constructs 140x140 cells in size were performed using Equations 3-6 through 3-11, with a non-dimensional propagation rate $\alpha = 1000$. The resulting kinetics of IIF are compared with theoretical predictions obtained using Equations 2-22 and 5-1 in Figure 5.1. It is evident that the analytical model is unable to accurately predict the transformation kinetics in the simulated 2-D tissue system.

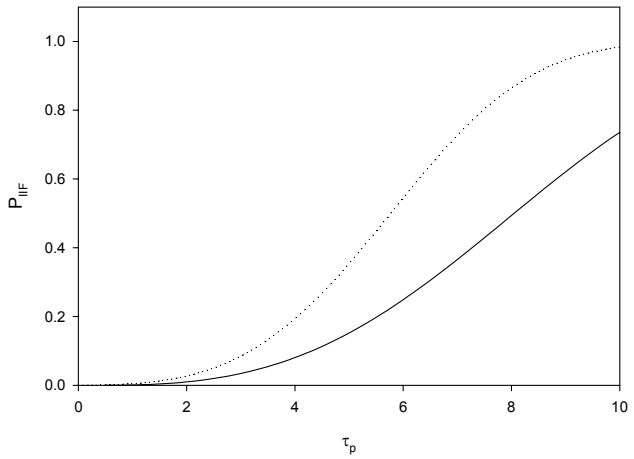

Figure 5.1. Comparison of Monte Carlo model for tissue constructs 140x140 cells in size for α = 1000 (dotted line) to the 2-D JMA model in Equation 5-1 (solid line).

5.2.2 Circular Geometry with Constant Growth Velocity

Whereas the growth process of the IIF domains does not proceed at a constant velocity in each lattice direction, the growth law for square geometry of the transformation domains, used by Weinberg and Kapral (1989), was not appropriate for our system. Instead, we assumed that the transforming domains would have an approximately circular geometry (prior to impingement), and initially considered a constant non-dimensional growth rate in the radial direction. Thus, we modeled each transformed domain as a circle of radius

$$R = \int_0^t J_p \, dt + \frac{1}{\sqrt{\pi}} \tag{5-2}$$

where a nonzero initial radius has been used, to account for the cell which nucleated the growth process. The growth law is then given by

$$n_0(\tau_p) = \pi R^2 \tag{5-3}$$

Using Equation 2-4 to non-dimensionalize Equation 5-2, we obtain

$$n_0(\tau_p) = \pi \tau_p{}^2 + 2\sqrt{\pi}\tau_p + 1 \tag{5-4}$$

As expected, $n_0(0) = 1$, representing the finite-sized initial nucleus. The extended transformed fraction follows from Equation 5-4:

$$P_{IIF}^e = \frac{\pi}{3\alpha}\tau_p{}^3 + \frac{\sqrt{\pi}}{\alpha}\tau_p{}^2 + \frac{1}{\alpha}\tau_p \tag{5-5}$$

5.2.3 Circular Geometry with Nonlinear Growth Rate

We recognized that the circular geometry assumed in Section 5.5.2 may not be accurate in the initial stages of growth, during which the square geometry of the underlying lattice is likely to have a significant effect on the growth process. Futhermore, whereas the microscale structure of the growth front is not planar, even for large transformed volumes, the radial growth velocity may not be linear. Thus, we developed a modified model for circular growth.

To obtain the growth law, we consider the circular geometry described by Equation 5-3, but write the following equation describing the number of additional IIF events occurring due to intercellular ice propagation in the infinitesimal time interval d*t*:

$$dn_o = 2\pi R\bar{k} \cdot J_p \cdot dt \tag{5-6}$$

where $\bar{k}$ is the average number of exposed interfaces per cell along the perimeter of the circular transformed region ($1 \leq \bar{k} \leq 4$ for a square lattice). Converting Equation 5-6 to non-dimensional form using Equation 2-4, and combining it with Equation 5-3, one can integrate the rate equation as follows:

$$\int_{n_0^*}^{n_0} \frac{1}{2} n_0^{-1/2} dn_0 = \int_{\tau_p^*}^{\tau_p} \sqrt{\pi} \cdot \bar{k} d\tau_p \tag{5-7}$$

The lower limits of integration in Equation 5-7 represent the earliest timepoint τ_p* at which the above assumptions hold, and the corresponding number of cells n_0* in the transformed region at this time. We will extrapolate the growth law obtained from Equation 5-7 for transformation times $0 \leq \tau_p \leq \tau_p$*. However, if

$$\tau_p^* > \frac{1}{\bar{k}} \sqrt{\frac{n_0^*}{\pi}} \tag{5-8}$$

then the extrapolated growth law can predict negative radii for the transformed region for small τ_p . To avoid this problem, we set R = 0 if a negative radius is predicted in the extrapolation zone. Thus, integration of Equation 5-7 yields

$$\sqrt{n_o} = \begin{cases} a\,\tau_p + b & \text{if } \tau_p \geq \dfrac{-b}{a} \\ 0 & \text{if } \tau_p < \dfrac{-b}{a} \end{cases} \tag{5-9}$$

where

$$a = \sqrt{\pi}\cdot\bar{k} \tag{5-10}$$

$$b = \sqrt{n_0^*} - \sqrt{\pi}\cdot\bar{k}\,\tau_p^* \tag{5-11}$$

Substituting the square of Equation 5-9 into Equation 2-21, one obtains

$$P_{IIF}^e = \begin{cases} \dfrac{a^2}{3\alpha}\tau_p^3 + \dfrac{ab}{\alpha}\tau_p^2 + \dfrac{b^2}{\alpha}\tau_p - \dfrac{b^2}{3\alpha}\cdot\max\left[-\dfrac{b}{a},0\right] & \text{if } \tau_p \geq \max\left[-\dfrac{b}{a},0\right] \\ 0 & \text{if } \tau_p < \max\left[-\dfrac{b}{a},0\right] \end{cases} \tag{5-12}$$

In order to estimate the values of the parameters a and b in Equation 5-12, we performed numerical experiments to estimate the growth law $n_0(\tau_p)$. Monte Carlo

simulations were performed using Equations 3-6 through 3-11 for tissues with dimensions 200x200 cells, with a single pre-existing frozen cell in the center of each tissue. Cells were allowed to freeze only by propagation, and the simulation was stopped when ever any cell at the tissue boundary froze. The function $n_0(\tau_p)$ was then estimated by averaging results from 180 simulations; the resulting kinetics are shown in Figure 5.2.

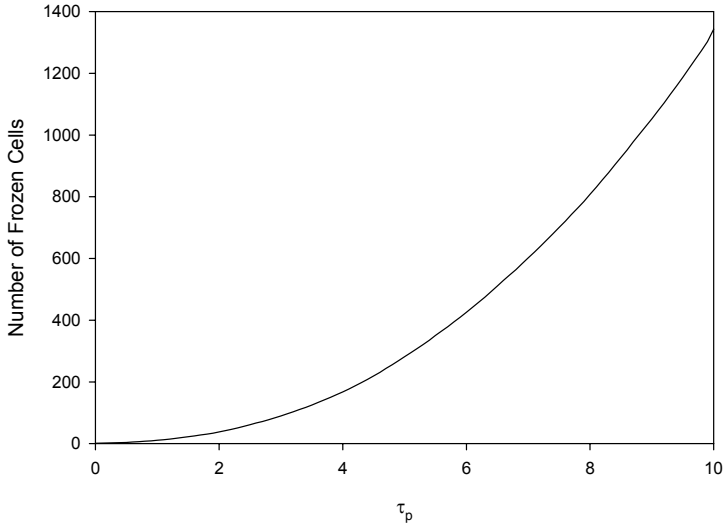

Figure 5.2. The kinetics of ice propagation initiated by a single frozen cell in 2-D tissue, predicted by Monte Carlo simulations in an ensemble of tissue constructs 200x200 cells in size.

To determine values for parameters *a* and *b* in Equation 5-9, the numerical data from Figure 5.2 were transformed by graphing $\sqrt{n_0}$ as a function of non-dimensional time τ_p, as shown in Figure 5.3. The resulting curve is approximately linear in the region $4 < \tau_p < 9.5$, and thus we let $\tau_p^* = 4$, and performed a linear regression using data in the

linear regime. The best-fit line was calculated for this range of τ_p (Figure 5.3) with $R^2 = 0.99$. The resulting best-fit parameters were $a = 3.91$ and $b = -2.80$ ($R^2 = 0.99$), and thus Equations 5-10 and 5-11 could be used to estimate $\bar{k} = 2.21$ and $n_0^* = 165$. In the growth law as described in Equation 5-9, $n_0 = 0$ for $0 \leq \tau_p \leq 0.72$ in order to prevent negative radii.

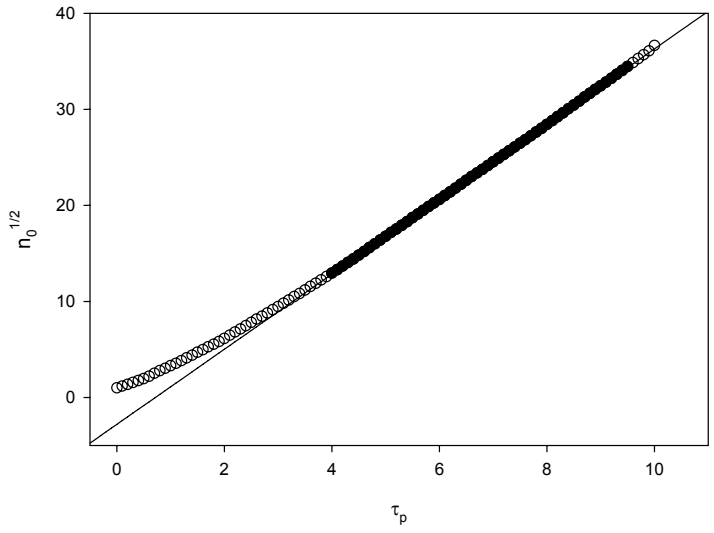

Figure 5.3. Determination of parameters *a* and *b* in Equation 5-9 by linear curve-fit (solid line) to empirical data (open symbols). The linear portion of the curve (filled symbols) was used in the linear regression.

5.2.4 Phenomenological Growth Law

Due to the questionable validity of the assumptions required for derivation of mechanistic growth laws, we also used a phenomenological growth law which did not make any assumptions about the geometry or mechanism of growth of the transformed regions. For consistency with JMA kinetics, we assumed a power law of the form

$$n_0 = c\tau_p^m + 1 \tag{5-13}$$

The parameters c and m were found from a linear regions of the numerical $n_0(\tau_p)$ data in Figure 5.2, after a logarithmic transformation, as shown in Figure 5.4. As seen in Figure 5.4, Equation 5-13 described the kinetics of transformation well for $\tau_p > 0.5$. Only the first five data points were excluded from the curve fit, yielding best fit parameters $c = 9.02$ and $m = 2.15$ ($R^2 = 0.99$). The extended transformed fraction was then obtained from Equation 5-13 using Equation 2-21:

$$P_{IIF}^e = \frac{c}{\alpha(m+1)} \cdot \tau_p^{\,m+1} + \frac{1}{\alpha}\tau_p \tag{5-14}$$

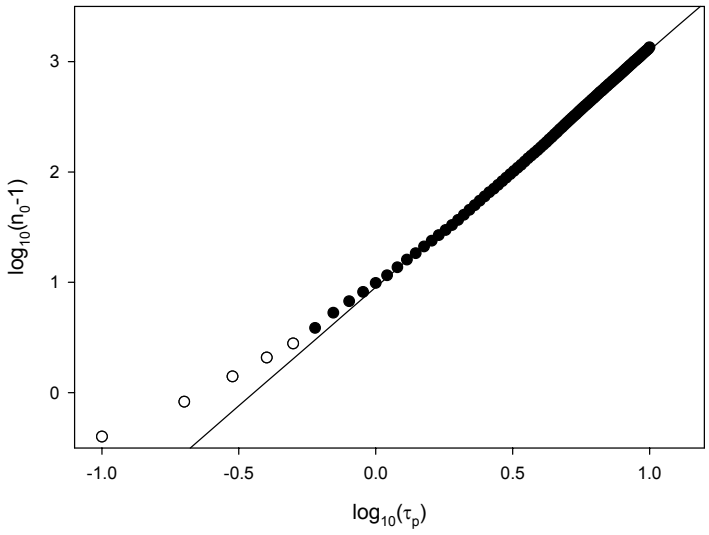

Figure 5.4. Linear curve-fit of Equation 5-13 to empirical growth law data (closed symbols), transformed as shown. The first five data points were excluded (open symbols).

5.2.5 Evaluation of 2-D JMA Models

To evaluate the four different 2-D JMA models developed above, we used the empirical growth law data from Figure 5.2 directly in Equation 2-21 by numerically integrating the Monte Carlo data using the trapezoidal rule. The resulting values for the extended probability of IIF were then transformed using Equation 2-22 to obtain a standard for comparison to the various model predictions.

In Figure 5.5, predictions from the four JMA models for $\alpha = 1000$ are compared to the standard curve derived from numerical experiments. The two models which assumed constant growth velocity yielded the worst predictions. Of the two models with non-

linear growth rates, the phenomenological model (Equation 5-14), yielded the best results. Thus, this model was used for all further analysis.

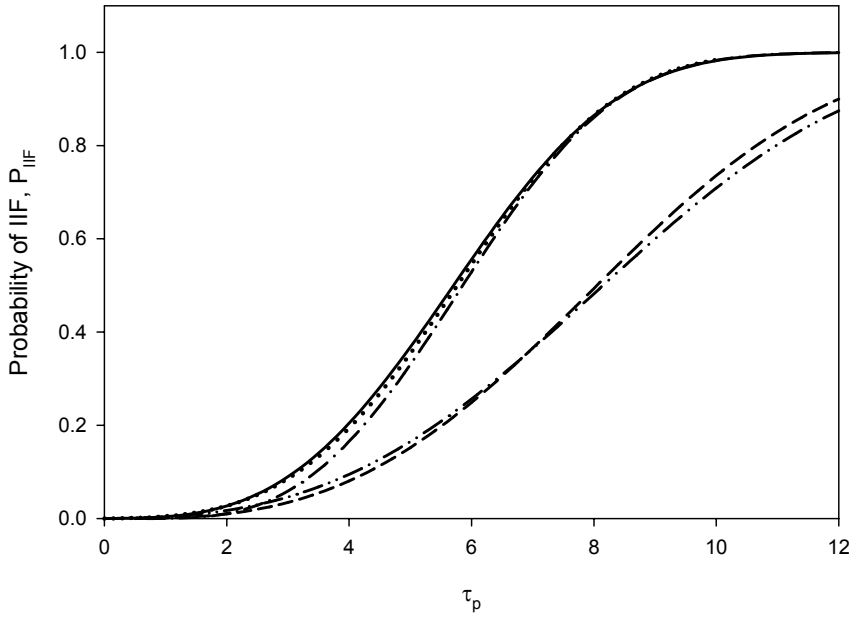

Figure 5.5. Comparison of empirically derived IIF kinetics in 2-D tissue with α = 1000 (dotted line), with theoretical predictions from constant growth rate models with square (Equation 5-1, dashed line) or circular geometry (Equation 5-5, dash-double-dotted line); nonlinear growth rate model with circular geometry (Equation 5-12, dash-dotted line); phenomenological power law model (Equation 5-14, solid line).

5.3 Effect of Finite Tissue Size on Predicted IIF Kinetics in 2-D Tissue

Because the finite-size effect was demonstrated to have a strong effect on transformation kinetics in 1-D tissues, Monte Carlo simulations of IIF in 2-D tissues of various sizes were compared to predictions from our 2-D JMA model (Equation 5-14).

Monte Carlo simulations were performed for the case of continuous nucleation with α = 100 or α = 1000, using Equations 3-6 through 3-11. For both values of α, Monte Carlo simulations were run for an ensemble of 300 tissues 35x35 cells in size, 150 tissues 70x70 cells in size, and 80 tissues 140x140 cells in size. Predicted IIF kinetics for α = 100 are shown in Figure 5.6. As the tissue size increases, the transformation kinetics observed in the Monte Carlo simulations more closely match predictions for the JMA model (which assumes infinite tissue size). Nonetheless, even for the largest tissue simulated (140x140 cells), the JMA model predictions and the Monte Carlo predictions diverged after ~ 30% transformation of the tissue. The discrepancy is due to the retardation of growth near the tissue boundaries, due to edge effects such as those described in Section 2.4. As shown in Figure 5.7, the mismatch between the JMA model predictions and to Monte Carlo simulations are worse when the intercellular ice propagation rate is increased to α = 1000; the IIF kinetics predicted by Monte Carlo simulations for 140x140 tissue diverge from JMA model predictions when less than 10% transformation has occurred. This observation is consistent with trends observed in Chapter 4, resulting from edge effects in 1-D tissues. Because the computational complexity of the Monte Carlo simulations was on the order of $O\{n_{cells}^2\}$, it was prohibitively costly to simulate IIF in larger tissues, which would be required in order to match the JMA model predictions.

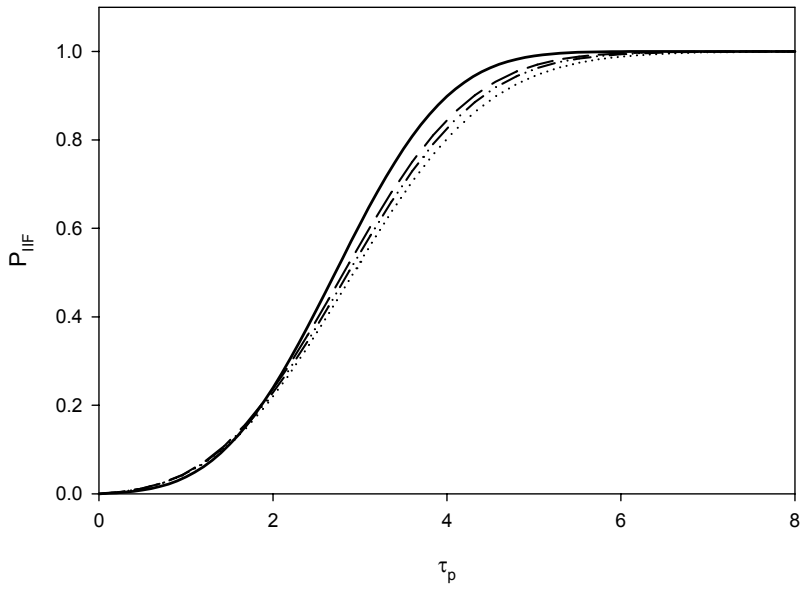

Figure 5.6. Demonstration of size-effect by comparison of Monte Carlo simulations of tissues 140x140 (long dash), 70x70 (dash-dot), and 35x35 (dot) cells in size with $\alpha = 100$ to 2-D JMA model (solid).

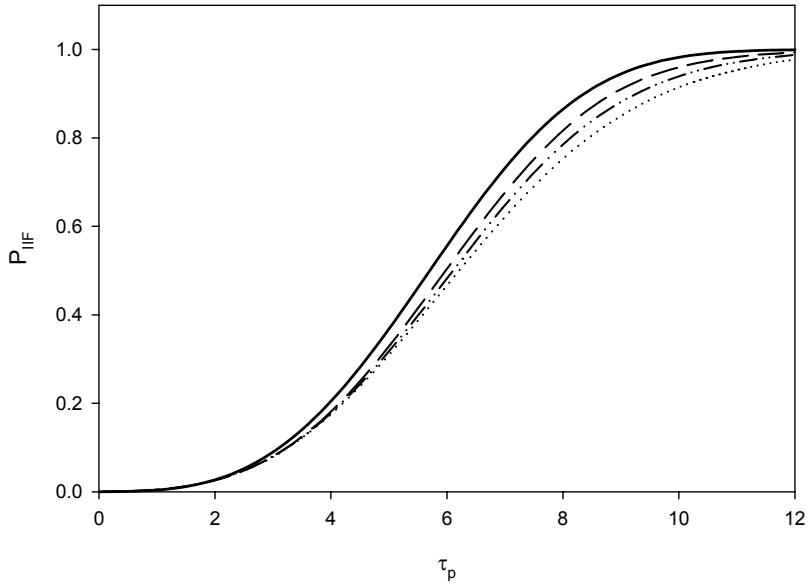

Figure 5.7. Demonstration of size-effect by comparison of Monte Carlo simulations of tissues 140x140 (long dash), 70x70 (dash-dot), and 35x35 (dot) cells in size with α=1000 to 2-D JMA model (solid).

Because the model presented by Weinberg and Kapral assumed a finite thickness only in one dimension, and assumed transformation with square tissue geometry and constant growth rates, their approach could not be used to correct for finite size effects in 2-D tissues. In order to develop a predictive rule for the effect of finite tissue size on transformation kinetics, trends were evaluated in the parameters of phenomenological models fit to Monte Carlo simulations of tissues of various sizes and propagation rates. Monte Carlo simulations were performed for α = 10, 100, and 1000 with tissues 35x35, 70x70, and 140x140 cells in size. The Monte Carlo models for these simulations were based on 300 simulations of 35x35 sized tissues, 150 simulations of 70x70 sized tissues, and 80 simulations of 140x140 sized tissues. The logarithmic transformations of the

Monte Carlo models were linearly curve-fit to the 2-D JMA model (Equation 5-14) and values for c and m determined (Figure 5.8 and 5.9). Values for c were generally higher than the theoretical value of c = 9.02, but no significant dependence on α or n_{cells} was seen. As predicted by the size-effect phenomenon, best-fit values for m were all lower than the theoretical value of m = 2.15. Following the expected trend, the value of m moved closer to the theoretical value as tissue size and α increased. This trend suggests that Monte Carlo models of tissues of adequate size would indeed match the 2-D JMA model.

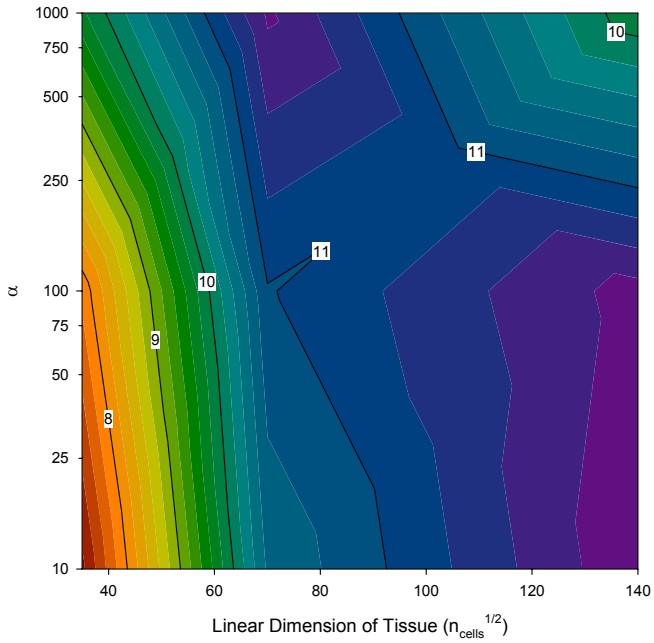

Figure 5.8. Values of best-fit parameter c from the phenomenological 2-D JMA model based on Monte Carlo simulations for α = 10, 100, 1000 and tissues 35x35, 75x75, and 140x140 cells in size.

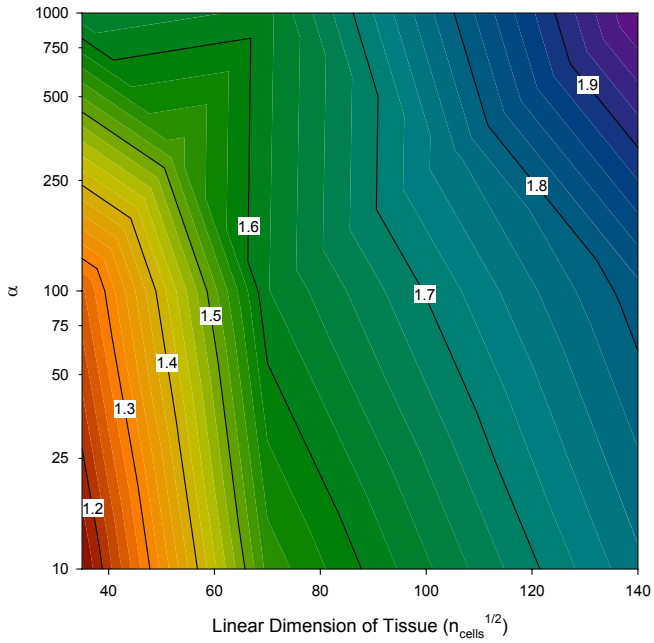

Figure 5.9. Values of parameter *m* from 2-D JMA model based on Monte Carlo simulations for α = 10, 100, 1000 and tissues 35x35, 75x75, and 140x140 cells in size.

Going back to our original hypothesis, that IIF in tissue constructs would be well described by a JMA equation of the form shown in Equation 2-24, we determined the effective Avrami coefficient and Avrami coefficient by combining Equations 2-22, 2-24, 2-5, and 2-14:

$$k = \frac{\alpha^m c}{m+1} \tag{5-15}$$

and

$$n = m + 1 \tag{5-16}$$

The data shown in Figure 5.8 and 5.9 were converted using Equations 5-15 and 5-16, and the resulting effective Avrami model parameters are shown as a function of α and tissue size in Figure 5.10.

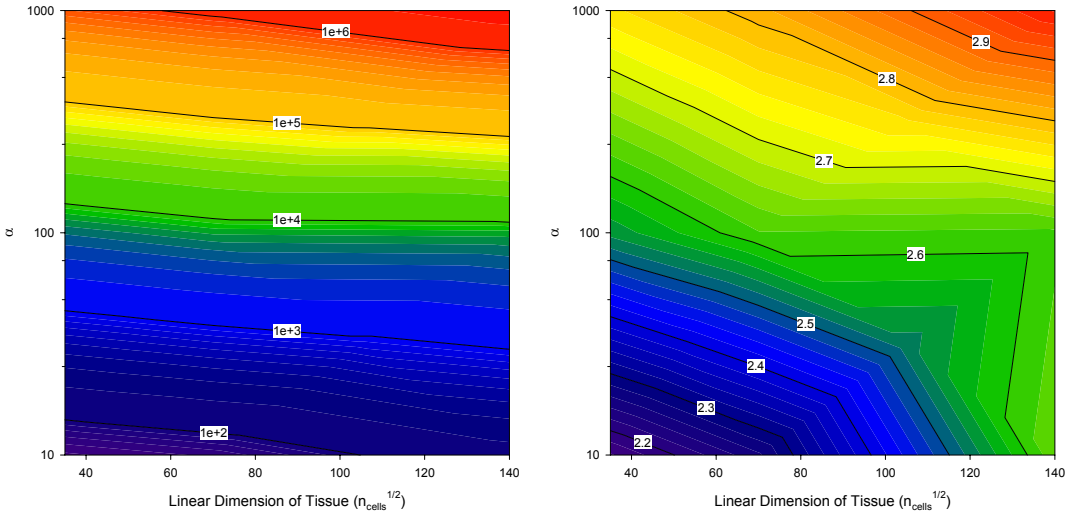

Figure 5.10. Values of parameter *k* (a) and *n* (b) from 2-D JMA model based on 2-D Monte Carlo simulations for α = 10, 100, 1000 and tissues 35x35, 75x75, and 140x140 cells in size.

The relationship of the JMA variables, k and n in Equation 2-24, to Monte Carlo simulation parameters was not as straightforward as with 1-D tissues. Whereas $k = \alpha$ for the 1-D case, k for the 2-D simulations ranged from $\alpha^{1.6}$ to $\alpha^{2.2}$ depending on tissue size. In the same vein, $n = 2$ for the 1-D case, while n ranged from 2.15 to 2.98 and increased with tissue size and α in the 2-D case.

5.4 Experimental Data

HepG2 cells are approximately 10 μm in diameter, so roughly 1600 cells span a confluent 16 mm circular coverslip. Because a simulated tissue size of 1000 cells was sufficient to approximate an infinite-sized system and match the JMA model for 1-D tissues, the number of cells in a monolayer on the coverslip was considered adequate to satisfy the infinite-size assumption of the 2-D JMA model.

Temperature and P_{IIF} data were collected from 13 freezing experiments, described in Section 3.2, with 1211 observed freezing events (Figure 5.11).

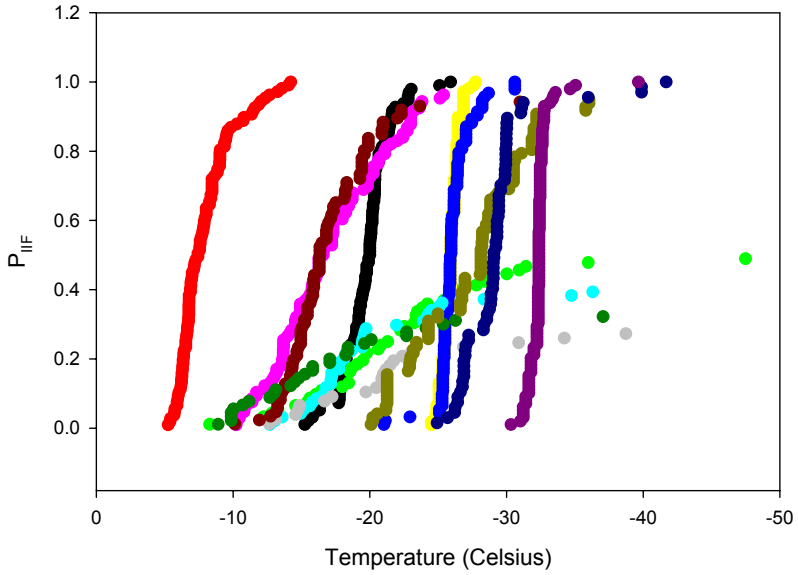

Figure 5.11. Plots of temperature and P_{IIF} of thirteen freezing experiments with a total of 1211 individual freezing events.

Frozen fractions for the experiments could be seen to fall into one of two categories: either freezing to >90% (Group A) or freezing to <60% (Group B). Digital images of freezing experiments in each category were reviewed and the freezing events described as either a result of nucleation if surrounded by unfrozen cells or a result of propagation if the cell was in contact with at least one frozen cell. The percent of freezing events resulting from propagation was >90% in Group A and <60% in Group B. The rate of nucleation-induced freezing events seemed to be consistent across all samples, while the capacity for ice to propagate between cells was greatly reduced in the Group B samples. One possible explanation may be an alteration in function of cellular gap-junctions known to play a direct role in the propagation of ice (Irimia and Karlsson, 2002). Because the biophysical response to assumed identical freezing conditions was vastly different between groups, only experiments freezing to >90% (Group A) were included in analysis of experimental data.

The cumulative frozen fraction (P_{IIF}) across experiments (total freezing events $n = 858$) was found and the temperature scale transformed to a non-dimensional time scale (τ) as described by Irimia and Karlsson (2002). This data was fit to the general form of the 2-D JMA equation (Equation 2-24) and values for k and n were determined to be 0.192 and 0.447, respectively. These values were much lower than the simulation-predicted values. Based on these values of equation parameters, the general form of the 2-D JMA equation was compared to the experimental data (Figure 5.12).

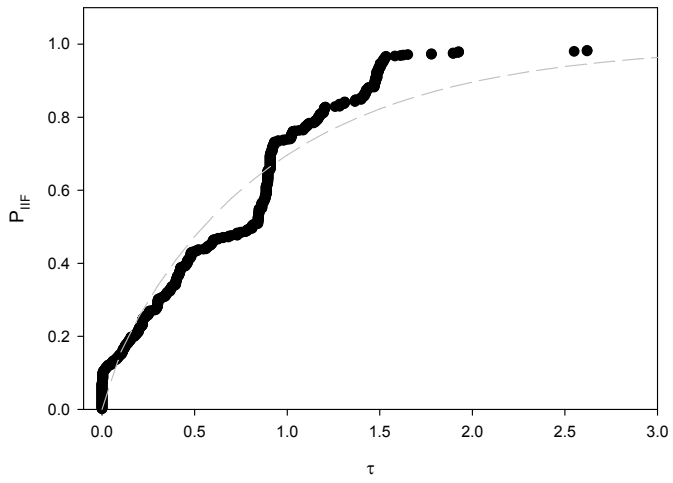

Figure 5.12. A comparison of the 2-D JMA equation (Equation 2-24) with experimentally determined values of k = 0.192 and n = 0.447 (dashed gray line) to experimental data (symbols).

Using the experimentally determined value of n = 0.447 substituted into Equation 5-16, α = 0.114 for HepG2. Alternatively, using the theoretical value of m + 1=3.147 from the 2-D JMA model in Equation 5-16 gives α = 0.284 for HepG2. These values of the non-dimensional propagation rate, α, are approximately one order of magnitude lower than that determined experimentally by Irimia and Karlsson (2002).

Even though Monte Carlo simulations have been shown to correctly predict IIF in experimental 2-cell systems (Irimia and Karlsson, 2002), experimental data from freezing experiments of HepG2 confluent monolayers were not well matched by the Monte Carlo simulation data in this case. Whether this is due to issues with the model (*i.e.*, assumptions) or issues with sample preparation (*i.e.*, variation between experiments) is unknown, but is left for Chapter 6 for discussion.

CHAPTER 6

DISCUSSION

6.1 Application of the JMA model to IIF in Tissues

In the present work, the JMA model was adapted and used to describe the kinetics of IIF during freezing of confluent biological tissues, thus greatly reducing the computational complexity. Given that the JMA model was derived for isothermal transformations in continuous media, the present approach hinged on two assumptions: (1) that the number of cells in the tissue is sufficiently large that a continuum approximation can be made; (2) that the kinetics of transformation conform to the JMA model, even though the freezing process is non-isothermal. The first of these assumptions does not appear to pose a significant problem; as shown in Section 4.3, predictions using a continuum model actually appear to improve with decreasing tissue size, as long as the JMA model is adapted to take into account edge effects due to the finite transformation domain (*e.g.*, using the WK model).

Whereas the classic JMA model (Equation 2-13) is typically used only to analyze the kinetics of transformation under isothermal conditions, we have applied it to a system in which freezing occurs non-isothermally, at a constant rate of temperature change. However, as demonstrated in Avrami's original treatise (Avrami, 1940), transformation kinetics under non-isothermal conditions can in fact be described by adapting the results from the analysis of isothermal transformations, if the system is an "isokinetic" regime. Transformations are isokinetic if the rates of nucleation and growth are proportional (*i.e.*, their ratio, α, is constant). It has previously been shown that for IIF in rapidly frozen

HepG2 tissue (the system used in the present experimental studies), the non-dimensional propagation rate α is approximately constant (Irimia, 2002; Irimia and Karlsson, 2002). Thus, it is reasonable to assume that isokinetic conditions prevail, and that the JMA model (or its modifications as presented here) will therefore adequately describe the non-isothermal kinetics of IIF.

It is possible that IIF occurring at slower rates of cooling (for which time-varying intracellular water concentrations are expected, as a result of dehydration), or in different cell types, may not be isokinetic, in which case the JMA formalism will strictly not be appropriate for analysis of IIF kinetics under conditions of non-isothermal freezing. Nonetheless, it has been shown that even under non-isothermal conditions, Equation 2-13 can be used to describe experimentally measured transformation kinetics, at least in limited temperature ranges (*e.g.*, Cebe, 1988; Krüger, 1993; Herrero and Acosta, 1994). Whereas the Avrami coefficient and exponent can generally not be interpreted in the context of the microscale mechanism of transformation under non-isothermal conditions (Di Lorenzo and Silvestre, 1999), in some cases a simple interpretation of the significance of k and n for non-isothermal kinetics can be derived (Woldt, 1992). Moreover, the Avrami exponent n obtained under isokinetic conditions is not very sensitive to temperature-dependence of α (Nakamura, *et al.*, 1973); *i.e.*, it may be possible to use the JMA model for cases of small to moderate deviations from the isokinetic regime.

For situations under which the JMA model is not valid, alternative models have been presented in the literature to handle non-isothermal transformation kinetics. For example, Ziabicki (1967) and Krüger (1993) have proposed that a non-isothermal transformation

be interpreted as a sequence of isothermal processes alternating with instantaneous step changes in the temperature. Others have derived extensions of the JMA model applicable to non-isothermal transformations and devised methods to estimate the Avrami parameters *k* and *n* based on analysis of non-isothermal data (Ozawa, 1971; Kissinger, 1957; Henderson, 1979). In principle, it should be possible to adapt one of these models to describe the kinetics of IIF in tissues, if conditions are encountered for which the isokinetic approximation is not adequate.

6.2 1-D Tissues

Several theories have been developed to predict the JMA transformation kinetics in finite-sized systems. For example, Yu and Lai (1995, 1996) derived an alternative JMA model for large one-, two-, and three-dimensional volumes using a finite discrete system and avoiding the concept of phantom volumes. Tagami and Tanaka (1996) developed a model of transformation kinetics in thin layers by adjusting the growth of phantom volumes. Sessa *et al*. (1996) validated the use of JMA in finite systems using a Monte Carlo model for various nucleation conditions in a lattice. In 1996, Cahn developed the purely analytical "time cone" method for determining transformed fractions in finite, inhomogeneous systems with changing boundary conditions and variable nucleation and growth rates. Levine and coworkers (1997) developed an analytical model to describe 3-D growth of spherical crystals in spherical and cubic systems and validated their model with Monte Carlo simulations. Using a numerical model, Pusztai and Granasy (1998) predicted the growth of grains with varying levels of anisotropy in finite systems. Implementing a probabilistic model of isotropic growth in 1-, 2-, and 3-D lattices,

Weinberg and Kapral (1989) considered JMA kinetics with growth restricted in one plane. The Weinberg-Kapral model was ultimately chosen for application to our 1-D Monte Carlo model because the WK discrete space and time system was easily adapted to our 1-D discretized tissue constructs.

The WK theory has been shown to more closely match the Monte Carlo predictions of IIF in 1-D tissues for certain simulation conditions. The predictions of the WK model more closely match those of the Monte Carlo model for higher α values holding tissue size constant (Figure 4.7). The error seen for low α values is a direct result of the WK discretized time step for several reasons. The WK model assumes that all nucleation events occurring during a given time interval happen at the start of that interval, and consequently, the WK model overestimates the transformed volume. This overestimation is related to the non-dimensional propagation rate, α. Because the seeding probability r is related to α as the inverse (Equation 2-55), values of $\alpha \leq 1$ cannot be assumed by the WK model. As α decreases, each discrete time interval covers a larger percentage of the time required for complete transformation, and as a result, the margin of error between the WK and Monte Carlo models increases as α approaches the lower bound. On the other hand, as α increases, the time step becomes very small with respect to the time for total transformation, and error caused by assuming nucleation at the start of the time step becomes increasingly insignificant. For future models, a better approximation of the nucleation and subsequent growth during a specific time interval for lower α values would be to assume that the nuclei form throughout the discrete time interval as described by Levine *et al*. (1997). For constant α, the error between the WK and Monte Carlo

models was seen to increase as tissue size increased. This trend is believed to be a result of the reduced number of simulations that could be performed for larger tissue sizes.

The results of our analysis showed that the finite size effect was more pronounced for smaller numbers of seed nuclei in the zero nucleation case. In Figure 4.5, for both $n_{cells} = 100$ and 1000, the difference between the JMA model and the MC and WK models was much larger for $p = 0.005$ than for the $p = 0.1$ case. Levine *et al*. do not see this trend in decrease of size-effect with increase in number of initial nuclei. However, it is unlikely that a change in size effect would be detected with the small increase (from 2 to 7) in number of nuclei tested in the Levine model, whereas the seeding probability was increased 20 fold for our analysis. Our work ultimately supports the claim of Levine *et al*. that the finite-size solution converges with the JMA model for the zero nucleation if the number of initial nuclei per tissue is very large, as seen in Figure 4.5 for both $p = 0.1$ cases.

As seen in Figure 4.8, the size-effect increases with increasing α for a constant tissue size. Increasing α, by definition (Equation 2-3), is equivalent to decreasing nucleation rate. Thus, our findings were again in support of the findings of Levine and coworkers who reported an increase in size-effect with a decrease in nucleation rate.

Although size-dependent divergences from the JMA model in our analysis were strong, Sessa *et al*. (1996) claim that with or without periodic boundary conditions in model simulations no size-effect could be seen and that data matched the predictions of the JMA model in all instances. However, upon converting the Sessa model parameters to the parameters used in our MC and JMA models, values of the propagation rate used by Sessa and coworkers were determined to be $\alpha << 1$. Based on our findings that size-

effect is less significant with smaller α values, as seen in Figure 4.7, the predictions of the Sessa model for their chosen lattice sizes would not have shown size-effects for such small α values.

Our results indicate that size effects are significant in 1-D tissues when $n_{cells} << \alpha^{1/2}$. This relationship supports the claim in the work of Pusztai and Granasy (1998) that for a characteristic time, t^*, defined by

$$X^e(t^*) = 1 \tag{6-1}$$

no size effects will be seen if the number of frozen cells at that time $n_0(t^*) << n_{cells}$. Substituting our modified formula for the extended fraction transformed (Equation 2-20) gives

$$X^e = \alpha\tau^2 + \tau \tag{6-2}$$

which is approximately equal to

$$X^e \approx \alpha\tau^2 \tag{6-3}$$

when $\alpha\tau >> 1$. Setting Equation 6-3 equal to unity gives the characteristic time for our system

$$\tau^* = \frac{1}{\sqrt{\alpha}} \tag{6-4}$$

Approximating the number of frozen cells described by Equation 2-16 with $\tau_n = 0$ as

$$n_0 \approx 2\alpha\tau \tag{6-5}$$

and substituting in the characteristic time yields

$$n_0 = 2\sqrt{\alpha} \tag{6-6}$$

Thus, size effects were negligible when $n_{cells} >> n_0$ (t^*), in agreement with the results of Pusztai and Granasy (1998).

6.3 2-D Tissues

Developing a modified 2-D JMA model was unexpectedly difficult because the extended volume model (Equation 2-21) was highly divergent from predictions of the 2-D JMA for lattices (Equation 5-1). The divergence appears early in the transformation, indicating a problem with the assumptions of the growth kinetics of the model (Figure 5.1). The growth law of the WK theory models constant growth velocity in clusters with square geometry, which does not hold true for the growth modeled by the Monte Carlo simulations. For this reason, and because the WK model is based on transformation in a volume where growth is only limited in one direction, the WK model could not be compared to predictions of the Monte Carlo models for small-sized tissues. The non-linear growth predicted by the Monte Carlo theory is evident as the phenomenological

model exponent $m > 2$ (Equation 5-13). The consequence of this rapid cluster growth is a decidedly non-spherical cluster shape that is significant even in large scale tissues. This growth phenomenon further explains the poor fits exhibited by the initial theoretical models developed assuming square cluster geometry with constant growth velocity and circular cluster geometry with both constant and nonlinear growth velocities (Figure 5.5). For more accurate representation of realistic cluster growth, future models of growth in tissues will require a random network of cellular interaction, such as the system described by Barabasi and Albert (1999) and as opposed to the regular lattice of cells used for the Monte Carlo model. The final modified JMA model used for describing 2-D IIF kinetics was a general phenomenological model which made no assumptions of the growth kinetics predicted by the MC theory.

A finite-size effect could be seen by comparison of Monte Carlo predictions to the derived 2-D JMA model (Figures 5.6 and 5.7). This size-effect was also demonstrated by the increase in Avrami exponent n towards the theoretical value of $n = m+1 = 3.14$ as tissue size and α increase. Based on results presented in Figure 4.8 for 1-D tissues, no size effect should be seen in 2-D tissues with $n_{cells} \geq 30$ and $\alpha = 10$, $n_{cells} \geq 50$ and $\alpha = 100$, or $n_{cells} \geq 300$ and $\alpha = 1000$. However, the size-effect is evident in 2-D tissues for $n_{cells} = 140$ for $\alpha = 10$, 100, and 1000, contradicting the n_{cells}-α relationship established for the 1-D case.

There are several possible explanations for the apparent difference in the size-effect phenomenon between one- and two-dimensional models. The reduction in transformation rate for 2-D tissues may not actually be a result of the size-effect, but perhaps the result of non-linear growth rates (Van Siclen, 1996). Also, the n_0 model

(Equation 2-21) used to derive the 2-D JMA model may have overestimated the growth rate predicted by the Monte Carlo simulations. Or, most probably, size-effects in 2-D tissues may be "stronger" than in 1-D tissues due to restricted growth in multiple directions.

To further confound the problem of the 2-D model development, trends in best-fit values of c and m from Monte Carlo simulations (Figures 5.9 and 5.10) are not as trends in size-effects in 1-D tissues had predicted. No dependence on n_{cells} or α could be seen for values for parameter c. The discrepancy between the theoretical predictions for m and predictions of the MC simulations is greater for smaller values of α, again in direct contraction to trends seen in 1-D model analysis. The unexpected trends in c and m values paired with the "stronger" than expected size-effects suggest that the size-effect is not the sole mechanism involved in the reduction of transformation rate in 2-D tissues.

6.4 Experimental Results

A curve-fit of experimental results to our phenomenological JMA model for 2-D tissues (Equation 5-14) yielded lower than expected values for the Avrami coefficient k and Avrami exponent n. An experimental value of α has previously been determined to be ~10 for HepG2 (Irimia and Karlsson, 2002). Based on this value, k should fall in the range of 10 to 100; however, an experimental value of k was found to be 0.192, an entire order of magnitude lower than expected. Similarly lower than expected, the value of n was found to be 0.447 for HepG2 experimental data. The expected value of n ranged from $n \sim 2$ as predicted by Monte Carlo simulations for $\alpha = 10$ with the influence of size

effects (Figure 5.11) to a value of $n = 3$ as predicted by the classical theoretical 2-D JMA for infinite sized tissues described by Christian (1975).

One possible explanation for these low k and n values is a non-uniform expression of gap-junctions across the monolayer. Domains free of gap-junctions may have formed, the size of which would be determined by the relative size of the gap-junction expressing patches and not necessarily by the size of the entire monolayer as assumed. Thus, the size effect would be present and limit the ice formation kinetics over the entire sample, yielding reduced k and n values. Because no evidence of gap-junction free patches could be seen during cryomicroscopy experiments, the size of these patches must be much larger than the field of view, or > 100 cells. Lending support to the likelihood of patches, cells in the samples were not uniform in density across the surface of the coverslip. Regions of cells that coalesced earlier in culture grew to be more heavily populated than those merging later. Cell density has been shown to affect phenotype in HepG2 (Kelly and Darlington, 1989), which may account for the proposed patches of variation in gap-junction expression across the sample. Although the existence of patches of cells with low or no gap-junction expression may plausibly explain the low k and n values, the fact that patches must have been larger than 100 cells suggests that size-effect alone was not responsible for the large discrepancy between experimental and theoretical values of the Avrami coefficient and exponent.

Freezing experiments produced results that fell into two distinct groups: final frozen fraction >90% (dominated by ice propagation) and final frozen fraction < 60% (minimal ice propagation). The existence of these groups reflects the findings of Irimia and Karlsson (2002) that two mechanisms, described as “fast” and “slow”, are involved in the

ice kinetics in 2-cell constructs. We hypothesize that the group of tissues that froze to < 60% was controlled by the "slow" mechanism indicating a negligible rate of ice propagation, whereas the group that froze to >90% was controlled by the "fast" mechanism indicating an appreciable rate of ice propagation. Based on review of the images taken during freezing experiments, very few neighboring IIF events occurred in the group dominated by the slow mechanism. Irimia and Karlsson (2002) found that roughly 50% of their experiments exhibited the slow mechanism, substantially greater than the 30% falling into the "slow" group in our findings. However, our results were based on 13 freezing experiments, and increased experiment number is needed for an accurate comparison of our findings to those of Irimia and Karlsson.

The probability of IIF by nucleation was found to be the same in both groups of experimental data. An IIF event was labeled "nucleation" if the frozen cell was surrounded by unfrozen neighbors and labeled "propagation" if the cell was in contact with at least one frozen neighbor, a method of distinguishing IIF mechanisms used by Acker, *et al.* (2001). The probability of nucleation was estimated as the number of nucleation events per total number of cells in the tissue. Because the probability of nucleation was consistent in both groups, one can conclude that the factor that mediates propagation (*e.g.*, gap-junctions) does not affect the nucleation rate. This conclusion is consistent with claims of Irimia and Karlsson (2002) that nucleation rate is not affected by cell-cell contact.

Because the nucleation rate was roughly equivalent in both groups, we hypothesize that the slow group resulted from negligible gap-junction expression across the monolayers in those samples. Gap-junctions are known to be involved in ice propagation

in tissues (Irimia and Karlsson, 2002; Berger and Uhrik, 1996), and HepG2 are known to have aberrant gap-junctions and low levels of connexin expression (Yang, *et al*., 2003). As mentioned above, based on the unusually low equation parameters determined from experimental data (excluding experiments from the "slow" group), patches of cells with no or irregular gap-junction expression are believed to form in the samples. Perhaps tissues labeled as members of the slow group were extreme examples of the gap-junction free patches, with domains of reduced gap-junction expression much larger than the 100 cells seen in one field of view, and size possibility approaching the span of the coverslip. In addition, variation and reduction in gap-junction expression that resulted in the two-group effect may have been triggered by time in culture. Gap-junction expression has been shown to be affected by time in culture > 7 days for HepG2 (Kelly and Darlington, 1989). The effect of time in culture to this extent on gap-junctions was not tested by Irimia and Karlsson (2002) who performed all experiments in 48 hours or less. Future experimentation will require the testing of gap-junction expression and functionality in monolayers cultured under conditions mentioned in Chapter 3.

CHAPTER 7

CONCLUSIONS

The goal of this work was to develop and validate a continuum model of intracellular ice formation (IIF) in tissues, by analogy with the well-known Johnson-Mehl-Avrami (JMA) model of transformation kinetics. To this end, the transformation kinetics in 1-D tissue constructs were analyzed. Comparisons of Monte Carlo simulation data to the modified JMA model indicated that the continuum models for kinetics of transformation in 1-D tissues were in excellent agreement with predictions obtained using the Monte Carlo method. For large constructs and relatively small values of non-dimensional propagation rate α, the modified JMA theory works well at predicting IIF. For large values of α, edge effects reduced the rate of transformation in the tissue, causing the Monte Carlo model to diverge from the modified JMA models; however, transformation kinetics under these conditions were well predicted by the Weinberg-Kapral theory. Problems with the transformation models were seen for small α values (< 60) with small tissue size (< 30): the modified JMA model was inaccurate due to size effects, and the Weinberg-Kapral model was inaccurate due to discretization errors. However, transformation kinetics of tissues under these conditions can easily be simulated using the Monte Carlo model, as the model is not computationally expensive for these parameter values.

Ultimately, analysis of 1-D tissues affirmed the feasibility of approximating transformation kinetics in tissues with a continuum model. Although outside the scope of this work, future development of the continuum approximation model will require

validation of the modified JMA model through cryomicroscopy experiments performed with micropatterned linear tissue constructs.

Analysis of 2-D tissues proved challenging due to a non-linear cluster growth rate resulting from the lattice geometry assumed by the Monte Carlo model. A phenomenological growth law derived from Monte Carlo simulations was used in the development of the 2-D JMA model in attempt to circumvent this problem. Due to high computational cost, we were unable to simulate sufficiently large 2-D tissues to avoid size effects and, consequently, were unable to validate the phenomenological 2-D JMA model using Monte Carlo techniques. Preliminary experimental data were similarly inconclusive. While qualitative trends in experimental data appeared to follow predictions of the model reasonably well, estimates of the Avrami coefficient and exponent were smaller than expected.

Future work in the analysis of transformation kinetics in 2-D tissues will require further development of predictive models and improved means of validation. The Weinberg-Kapral model will need to be modified to consider four boundary planes to match the assumption of tissue geometry used in the Monte Carlo model and to predict consequent size effects. Alternatively, the Monte Carlo model will require modification to increase computational efficiency, thus allowing simulations to be performed for large tissues which would exhibit no size effect. Improvements in experimental techniques may prove insight into the unexpected values of the Avrami coefficient and exponent and provide validation of the modified JMA model.

In summary, the feasibility of using a continuum approximation to describe the transformation kinetics in tissue constructs has been demonstrated. Because the

developed model is not restricted by computational complexity, IIF in tissues of arbitrary size can be predicted.

REFERENCES

Acker, J.P., J.A.W. Elliot, and L.E. McGann. 2001. Intercellular ice propagation: experimental evidence for ice growth through membrane pores. *Biophys. J.* 81:1389-1397.

Acker, J.P., A. Larese, H. Yang, A. Petrenko, and L. E. McGann. 1999. Intracellular ice formation is affected by cell interactions. *Cryobiology* 38:363-371.

Acker, J.P., and L.E. McGann. 1998. The role of cell-cell contact in intracellular ice formation. *Cryo Lett*. 19:367-374.

Avrami, M. 1940. Kinetics of Phase Change: Tranformation-Time Relations for Random Distribution of Nuclei. *J. Chem. Phys*. 8:212-224.

Barabasi, A.L., and R. Albert. 1999. Emergence of Scaling in Random Networks. *Science* 286:509-512.

Berger, W.K., B. Uhrik. 1996. Freeze-induced shrinkage of individual cells and cell-to-cell propagation of intracellular ice in cell chains from salivary glands. *Experientia* 52:843-850.

Berger, W.K., B. Uhrik. 1992. Dehydration and intracellular ice formation during freezing in single cells and in cell strands from salivary glands. *Cryobiology* 29:715-716. (Abstr.)

Bischof, J. C., D. Smith, P.V. Pazhayannur, C. Manivel, J. Hulbert, and K.P. Roberts. 1997. Cryosurgery of Dunning AT-1 rat prostate tumor: thermal, biophysical, and viability response at the cellular and tissue level. *Cryobiology* 34 (1):42-69.

Boone, W.R., J.E. Johnson, D.W. Blackhurst, and H.L. Hidgon. 2004. Cryopreservation methodologies: Freezing location and protocol alter development of mouse embryos. *Cont. Topics Lab. Anim. Sci*. 43(1):26-31.

Bradley, R.M. 1987. Comment on "Ring dynamics and percolation in an excitable medium". *J. Chem. Phys*. 86(12):7245-7246.

Cahn, J.W. 1997a. Johnson-Mehl-Avrami Kinetics on a Finite Growing Dowman with Time and Position Dependent Nucleation and Growth Rates. *Trans. Indian Inst. Met*. 50(6)573-580.

Cahn, J.W. 1997b. Comment on: Reassessing the nucleation and growth kinetics of solid state phase transformations. *Mat. Res. Innovat*. 1:64-65.

Cahn, J.W. 1996. The time cone method for nucleation and growth kinetics on a finite domain. *Mat. Res. Soc. Symp. Proc*. 398:425-437.

Cebe, P. 1988. Non-isothermal crystallization of poly(etheretherketone) aromatic polymer composite. *Poly. Comp*. 9(4): 271-279.

Christian, J.W. 1975. "The Theory of Transformation in Metals and Alloys," 2nd ed. Pergammon, New York.

Clemente R.A., and A.M. Saleh. 2002. Crystallization kinetics: A solution for geometrical impingement. *Phys. Rev. B*. 65(13): art.no. 132102.

Devireddy, R.V., B. Fahrig, R.A. Godke, S.P. Leibo. 2004. Subzero water transport characteristics of boar spermatozoa confirm observed optimal cooling rates. *Mol. Rep. Devel*. 67(4):446-457.

Devireddy, R.V., P.R. Barratt, K.B. Storey, J.C. Bischof. 1999. Liver freezing response of the freeze-tolerant wood frog, Rana sylvatica, in the presence and absence of glucose. I. Experimental measurements. Cryobiology 38(4): 310-326.

Diller, K.R., and J.F. Raymond. 1990. Water transport through a multicellular tissue during freezing: A network thermodynamic modeling analysis. *Cryo Lett*. 112:151-162

Di Lorenzo, M.L., and C. Silvestre. 1999. Non-isothermal crystallization of polymers. *Prog. Polym. Sci*. 24:917-950.

Erukhimovitch, V., and J. Baram. 1994. Crystallization Kinetics. *Phys. Rev. B*. 50(9):5854-5856.

Fanfoni, M., M. Tomellini, and M. Volpe. 2002. Treatment of phantom overgrowth in the Kolmogorov-Johnson-Mehl-Avrami kinetics as a correlation problem. *Phys. Rev. B*. 65(17): art. no. 172301.

Foubert, I., K. Dewettinck, and P.A. Vanrolleghem. 2003. Modelling the crystallization kinetics of fats. *Trends in Food Sci Tech*. 14:79-92.

Gillespie, D.T. 1976. A General Method for Numerically Simulating the Stochastic Time Evolution of Coupled Chemical Reactions. *J Comp Phys*. 22:403-434.

Hayes, L.J., K.R. Diller, H.J. Chang, and H.S. Lee. 1988. Prediction of local cooling rates and cell-survival during the freezing of a cylindrical specimen. *Cryobiology* 25(1):67-82.

Henderson, D.W. 1979. Thermal Analysis of Non-Isothermal Crystallization Kinetics in Glass Forming Liquids. *J. Non-Crys. Solids* 30:301-315.

Herrero, C.R., and J.L. Acosta. 1994. Effect of poly(epichlorhydrin) on the crystallization and compatibility behavior of poly(ethylene oxide) polyphosphazene blends. *Polymer Journal* 26(7): 786-796.

Irimia, D., and J.O.M. Karlsson. 2004. Kinetics of Intracellular Ice Formation in One-dimensional Arrays of Interacting Biological Cells. *Biophys. J*. Submitted.

Irimia, D., and J.O.M. Karlsson. 2002. Kinetics and Mechanism of Intercellular Ice Propagation in a Micropatterned Tissue Construct. *Biophys. J.* 82:1858-1868.

Irimia, D. 2002. Effects of Cell-Cell and Cell-Substrate Interactions on Ice Formation in Micropatterned Tissue Constructs. *Doctoral thesis*. University of Illinois at Chicago.

Johnson, W. A., and R.F. Mehl. 1939. Reaction kinetics in processes of nucleation and growth. *Trans. Am. Inst. Min. Metall. Pet. Eng*.135:416-442.

Karlsson, J.O.M, and M. Toner. 2000. Cryopreservation. *In* "Principles of Tissue Engineering," 2nd ed.:293-307 Academic Press.

Karlsson, J.O.M., and M. Toner. 1996. Long-term storage of tissues by cryopreservation: critical issues. *Biomaterials* 17:243-256.

Karlsson, J.O.M., E.G. Cravalho, and M. Toner. 1993. Intracellular ice formation: Causes and consequences. *Cryo Lett*. 14:323-336.

Kashchiev, D. 2000. "Nucleation: Basic Theory with Applications". Butterworth-Heinemann, Oxford.

Kashchiev, D., and A. Firoozabadi. 1993. Kinetics of the initial stage of isothermal gas phase formation. *J. Chem. Phys*. 98:4690-4699.

Kelly, J.H, and G.J. Darlington. 1989. Modulation of the liver specific phenotype in the human hepatoblastoma line HepG2. *In Vitro Cell Dev. Biol*. 25(2):217-222.

Kissinger, H.E. 1957. Reaction kinetics in differential thermal analysis. *Anal. Chem*. 29(11):1702-1706.

Krüger, P. 1993. On the relationship between non-isothermal and isothermal KJMA crystallization kinetics. *J. Phys. Chem. Solids* 54(11):1549-1555.

Larese, A., H.Yang, A. Petrenko, and L.E. McGann. 1992. Intracellular ice formation is affected by cell to cell contact. *Cryobiology* 29:728. (Abstr.)

Levin, R. L., E. G. Cravalho, and C.E. Huggins. 1977b. Water transport in a cluster of closely packed erythrocytes at subzero temperatures. *Cryobiology* 14:549-558.

Levin, R.L, E.G. Cravalho, and C.E. Huggins. 1977a. Diffusion Transport in a Liquid Solution with a Moving, Semipermeable Boundary. *Trans ASME*. 99:322-329.

Markworth, A.J. 1984. Analysis of the Extent of Growth-Induced Impingement for a Simple Model of Precipitative Nucleation and Growth. *Script. Metall*. 18:1309-1311.

Mazur, P. 1984. Freezing of living cells: mechanisms and implications. *Am. J. Phys*. 247: C125-C142.

Mazur, P., S.P. Leibo, and E.H.Y. Chu. 1972. A Two-Factor Hypothesis of Freezing Injury: Evidence from Chinese Hamster Tissue-culture Cells. *Experim. Cell Res*. 71:345-355.

Mazur, P. 1965. The role of cell membranes in the freezing of yeast and other single cells. *Ann. NY Acad. Sci.* 125:658-676

Mazur, P. 1963. Kinetics of water loss from cells at subzero temperatures and likelihood of intracellular freezing. *J.Gen. Phys*. 47:347-369.

McGann, L.E., J. Kruuv, and H.E. Frey. 1972. Repair of freezing damage in mammalian cells. *Cryobiology* 9:496-501.

Michaelsen, C., M. Dahms, and M. Pfuff. 1996. Crystallization Kinetics. *Phys. Rev. B.* 53(17):11877-11877.

Muldrew, K., L. E. McGann. 1994. The osmotic rupture hypothesis of intracellular freezing injury. *Biophys. J*. 66:532-541.

Nakamura, K., K. Katayama, and T. Amano. 1973. Some Aspects of Nonisothermal Crystallization of Polymers. II. Consideration of the Isokinetic Condition. *J. Appl. Polym. Sci*. 17:1031-1041.

Ozawa, T. 1971. Kinetics of non-isothermal crystallization. *Polymer* 12:150-158.

Pineda, E. and D. Crespo. 1999. Microstructure development in Kolmogorov, Johnson-Mehl, and Avrami nucleation and growth kinetics. *Phys. Rev. B*. 60(5):3104-3112.

Pitt, R.E. and P.L. Steponkus. 1989. Quantitative analysis of the probability of intracellular ice formation during freezing of isolated protoplasts. *Cryobiology* 26:44-63.

Porsche, A.M., C. Korber, and G. Rau. 1991. Freeze thaw behavior of cultured (bovine corneal) endothelial cells: suspension and monolayer. *Cryobiology* 28:545. (Abstr.)

Pusztai, T., and L. Granasy. 1998. Monte Carlo simulation of first-order phase transformation with mutual blocking of anisotropically growing particles up to all relevant orders. *Phys Rev B*. 57(22):14110-14118.

Rabin, Y., M. J. Taylor, and N. Wolmark. 1998. Thermal expansion measurements of frozen biological tissues at cryogenic temperatures. *J. Biomech. Eng: Trans ASME*. 120:259-266.

Rall, W. F., P. Mazur, and J. J. McGrath.1983. Depression of the ice-nucleation temperature of rapidly cooled mouse embryos by glycerol and dimethyl sulfoxide. *Biophys. J*. 41:1-12.

Rubinsky, B. 1989. The energy equation for freezing biological tissue. *J. Heat Transfer* 111:988-997.

Schwartz, G.J. and K.R. Diller. 1983. Osmotic response of individual cells during freezing: 2. Membrane-permeability analysis. *Cryobiology* 20:542-552

Sessa, V., M. Fanfoni, and M. Tomellini. 1996. Validity of Avrami's kinetics for random and nonrandom distributions of germs. *Phys. Rev. B*. 54(2):836-841.

Srolovitz, D.J., G.S. Grest, and M.P. Anderson. 1986. Computer Simulation of Recrystallization-I. Homogeneous Nucleation and Growth. *Acta Metall*. 34(9):1833-1845.

Sumpter, M.L., S.L. Stott, and J.O.M. Karlsson. 2003a. Avrami Kinetics of Intercellular Ice Propagation during Freezing of Confluent Tissues (abstract and short-talk). *Cryobiomol 2003: Organs and Tissues Cryoprotection. Coimbra, Portugal, September 14-18, 2003.*

Sumpter, M.L., K.A. Carnevale, and J.O.M. Karlsson. 2003b. Avrami Kinetics of Simulated Intracellular Ice Formation in Confluent Tissues during Freezing (abstract and poster). *Program and Abstracts of ET2003: Engineering Tissues. Hilton Head, South Carolina, Feb 2003.*

Tobin, M.C. 1974. Theory of Phase Transition Kinetics with Growth Site Impingement. I. Homogeneous Nucleation. *J. Poly. Sci*. 12:399-406.

Toner, M. 1993. Nucleation of ice crystals inside biological cells. *In* "Advances in Low-Temperature Biology". Vol 2:1-51. JAI Press, London.

Toner, M., E.G. Cravalho, and M. Karel. 1990. Thermodynamics and kinetics of intracellular ice formation during freezing of biological cells. *J. Appl. Phys*. 67:1582-1592.

Toscano, W.M, E.G. Cravalho, O.M. Silvares, C.E. Huggins. 1975. The thermodynamics of intracellular ice nucleation in the freezing of erythrocytes. *J. Heat Transfer* 97 (3): 326-332.

Tsuruta, T., Y. Ishimoto, and T. Masuoka. 1998. Effects of glycerol on intracellular ice formation and dehydration of onion epidermis. *Ann. NY Acad. Sci*. 858:217-226.

Tunitskii, N. N. 1941. *Zh. Fiz. Khim*. 15:1061.

Van Siclen, C.D. 1996. Random nucleation and growth kinetics. *Phys. Rev. B*. 54(17):11845-11848.

Viskanta R., M.V.A. Bianchi, J.K. Critser, and D. Gao. 1997. Solidification Processes of Solutions. *Cryobiology*. 34(4):348-62.

Weibe, M.E. and L.H. May. 1990. Cell banking. *Bioprocess. Technol*. 10: 147-160.

Weinberg, M., and R. Kapral. 1989. Phase transformation kinetics in finite inhomogeneously nucleated systems. *J. Chem. Phys*. 91(11):7146-7152.

Woldt, E. 1992. The relationship between isothermal and nonisothermal description of the Johnson-Mehl-Avrami-Kolmogorov kinetics. *J. Phys. Chem. Solids*. 53(4): 521-527.

Yang, J., A. Ichikawa, and T. Tsuchiya. 2003. A novel function of connexin 32: marked enhancement of liver function in a hepatoma cell line. *Biochem. Biophys. Res. Comm*. 307:80-85.

Yu, G., and J.K.L. Lai. 1996. Kinetics of transformation with nucleation and growth mechanism: Two- and three-dimensional models. *J. Appl. Phys*. 79(7):3504-3511.

Yu, G., and J.K.L. Lai. 1995. Kinetics of transformation with nucleation and growth mechanism: fundamentals of derivation and one-dimensional model. *J. Appl. Phys*. 78(10):5965-5969.

Zhao, G., L.Q. He, P.T. Wang, W.P. Ding, X.J Xie, Z. Liu, H.F. Zhang, Z.Q. Shu, D.W. Luo, D.Y. Gao. 2003. Determination of cell volume during equilibrium freezing process. *Chin. Sci. Bull*. 48(15):1551-1554.

Ziabicki, A. 1967. *Appl. Poly. Symp*. 6:1.